ACS OMEGA

http://pubs.acs.org/journal/acsodf

Article

The Role of the Ferroelectric Polarization in the Enhancement of the Photocatalytic Response of Copper-Doped Graphene Oxide–TiO_2 Nanotubes through the Addition of Strontium

Nuhad Abdullah Alomair, Nouf Saleh Al-Aqeel, Sanaa Saad Alabbad, Hafedh Kochkar,* Gilles Berhault,* Muhammad Younas, Fathi Jomni, Ridha Hamdi, and Ismail Ercan

Cite This: *ACS Omega* 2023, 8, 8303–8319

Read Online

ACCESS | Metrics & More | Article Recommendations | Supporting Information

ABSTRACT: To evaluate the potential role of in situ formed Sr–Ti–O species as a ferroelectric component able to enhance the photocatalytic properties of an adjacent TiO_2 semiconductor, Cu-doped/graphene oxide (GO)/TiO_2 nanotubes (TiNTs) composites (with 0.5 wt % Cu and 1.0 wt % GO) have been synthesized while progressive amounts of strontium (up to 1.0 wt %) were incorporated at the surface of the composite through incipient wetness impregnation followed by post-thermal treatment at 400 °C. The different resulting photocatalytic systems were then first deeply characterized by means of N_2 adsorption–desorption measurements, X-ray diffraction (XRD), UV–vis diffuse reflectance (UV–vis DR), Raman and photoluminescence (PL) spectroscopies, and scanning electron microscopy (SEM) (with energy-dispersive X-ray (EDX) spectroscopy and *Z*-mapping). In a second step, optimization of the kinetic response of the Sr-containing composites was performed for the formic acid photodegradation under UV irradiation. The Sr-containing Cu/GO/TiNT composites were then fully characterized by electrochemical impedance spectroscopy (EIS) for their dielectric properties showing clearly the implication of polarization induced by the Sr addition onto the stabilization of photogenerated charges. Finally, a perfect correlation between the photocatalytic kinetic evaluation and dielectric properties undoubtedly emphasizes the role of ferroelectric polarization as a very valuable approach to enhance the photocatalytic properties in an adjacent semiconductor.

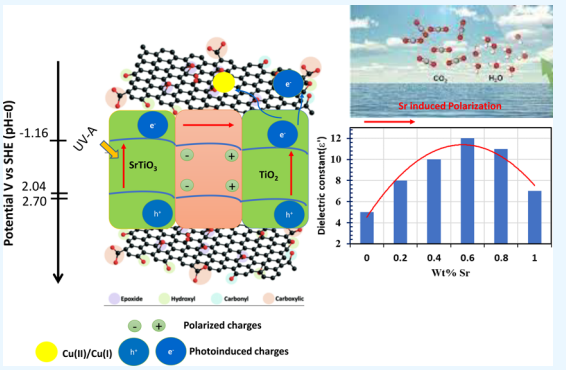

1. INTRODUCTION

Photocatalysis is a very effective advanced oxidation process (AOP) used to remove pollutants present in wastewater or the atmosphere. Photocatalysis can also be employed for the production of green energy (e.g., H_2 and C_1 production) or for the conversion of biomass sources.[1−3] Among the various applied semiconductors used in photocatalysis, titanium dioxide (TiO_2) shows a high photocatalytic efficiency and a strong oxidizing ability for the photodegradation of several pollutants and for the disinfection of various harmful compounds in both water and air applications.[4,5] However, TiO_2 presents two main drawbacks: (1) a large band gap (3.2 eV for anatase) leading to activation only in the UV range (λ < 385 nm) and therefore limiting its photoabsorption ability to only a small fraction of solar light (about 3–4%) and, (2) a quite high recombination rate of electron–hole pairs. These drawbacks limit the practical application of TiO_2.[6,7] Considerable efforts have then been made in extending its photoabsorption to visible light through doping and codoping by metals and/or nonmetals, coupling with metal oxides or through acid inorganic treatment of TiO_2.[1,8−18] Similarly, the rate of recombination of photogenerated carriers can be decreased by changing the morphology of titanium oxide to one-dimensional (1D) materials (films, tubes, wires, and rods),[19−22] by doping with earth metals[9−23] (La and Ce) or by combining TiO_2 with nanostructured carbon materials such as fullerenes, polyhydroxyfullerene, carbon nanotubes, or graphene oxide (GO) to form carbon–TiO_2 composites.[24−28] The design of cerium-doped TiO_2 nanomaterials with tuned structural and textural properties was previously reported.[23] Results emphasized the beneficial effect of cerium doping of TiO_2 nanotubes (TiNTs), the activity reaching 39 μmol·L^{-1}·min^{-1} against 16 μmol·L^{-1}·min^{-1} for Ce-free sample after calcination at 700 °C. This result is due to not only the redox properties of cerium but also a stabilization effect of the anatase phase at high calcination temperature (700 °C).

Received: October 18, 2022
Accepted: February 14, 2023
Published: February 24, 2023

Hence, the presence of Ce limits the growth of TiO_2 crystallite sizes during the post-thermal treatment. Similar results are reported for lanthanum-modified TiO_2 nanorods (NR), the photodegradation of formic acid under UV-A onto the lanthanum-doped sample being four times more active (k = 52 μmol·L^{-1}·min^{-1}) than the nondoped one (k = 13 μmol·L^{-1}·min^{-1}) after calcination at 700 °C.[28] Hamandi et al. showed that incorporating 1 wt % of poly(hydroxyfullerene) (PHF) onto TiO_2 nanotube helps to maintain surface oxygen vacancies at the TiO_2 surface as well as Ti^{3+} sites and to improve faradic current across the semiconductor interface leading to much better photocatalytic activity of formic acid.[29] More recently, Bin Sadi et al.[30] demonstrated that the photodegradation of formic acid is boosted in the presence of cyanuric acid-modified TiO_2 nanoparticles due to the creation of nitrogen defects as evidenced by PL measurements. The photodegradation of formic acid under UV-A onto 5 wt % cyanuric acid-doped TiO_2 is more than two times more active (k = 82.6 μmol·L^{-1}·min^{-1}) than TiO_2 P25 (k = 35 μmol·L^{-1}·min^{-1}).

The hybridization of TiO_2 with graphene oxide or reduced graphene oxide (rGO) impacts the band gap energy: due to this hybridization, the absorption threshold would shift from UV to the edge of the visible range.[31] Graphene oxide (GO) has attracted significant attention in the past few decades in photocatalysis applications due to its unique properties such as its high surface area, good thermal and electrical conductivities, and excellent charge carrier mobility.[31,32] Hence, combining TiO_2 nanotubes with GO results in the creation of new hydroxyl groups and oxygen vacancies influencing the charge carrier transfer.[31] In this respect, rGO was successfully obtained by GO photoreduced by $BiVO_4$ and provides a great improvement in the activity for water splitting by efficiently transferring photoexcited electrons from the O_2 photocatalyst to the H_2 photocatalyst. Based on UV-DRS and electrical measurements, the authors concluded that RGO acts as an electron conductor rather than as a semiconductor.[33] Kumbhakara et al.[34] also reported a green synthesis approach to synthesize in situ 2D rGO-ZnO (rGZn) nanocomposites from apple juice and zinc acetate. rGZn nanocomposites showed excellent efficiency (~60%) for the photodegradation of methylene blue (MB) under direct sunlight irradiation.

Other strategies were also investigated through, for instance, the inhibition of the photogenerated electron−hole recombination and the shifting of the absorption toward visible light by doping TiO_2 with transition metals such as Cu, Fe, Co, and Ni−Cu.[35] In this respect, copper is an interesting candidate since it possesses different degrees of oxidation leading to different oxide species on TiO_2, Cu_2O, and CuO being the main species observed. However, the exact nature (CuO or Cu_2O) of the copper oxide entities participating in the enhancement of TiO_2 photocatalytic properties remains debated.[36−39] Indeed, according to several reports, Cu_2O species were found to be more likely responsible for enhanced photocatalytic activity, while few other reports suggest that CuO is in fact responsible for a better separation of charge carriers (electrons and holes).[35,39,40] The exact role of copper was also debated. For instance, Yan et al. and Zhu et al. prepared Cu-doped TiO_2 nanoparticles (NPs) and demonstrated that Cu−TiO_2 exhibited smaller band gap values compared to pristine TiO_2.[41,42] Krishnakumar et al. reported that Cu doping inhibited recombination of photogenerated pairs of TiO_2 and boosted the photocatalytic activity.[43] Moreover, copper-doped TiO_2 with or without GO was found as an interesting alternative for enhanced photocatalytic systems. For instance, on Cu/TiO_2 nanotubes, Zghab et al.[44] evidenced unambiguously a stabilization of Cu NPs at a + I oxidation state due to a strong interaction with TiO_2 nanotubes leading to an 80% increase in activity for formic acid (FA) degradation under UV irradiation. When combined with GO, Zghab et al.[44] found that a synergetic effect between copper and graphene oxide deposited separately onto TiO_2 nanotubes can effectively improve the interfacial charge transfer processes limiting charge recombination. It also offers more adsorption sites leading to a better photocatalytic hydrogen evolution for solar water splitting applications.[45] Contrary to GO/TiO_2 nanotubes, in the presence of Cu, the addition of nonreduced GO leads to a 150% increase in activity compared to its free counterpart Cu/TiO_2 nanotubes while the use of partially reduced GO leads to a complete loss of any beneficial effect due to the creation of defects on the graphene layers allowing Cu to interact again directly with TiO_2.

Better separation of the photogenerated charges can also be obtained through the application of an electric field resulting from the energy mismatch at the semiconductor/electrolyte contact area. Indeed, varying the electronic band structure at the interface is an attractive approach to improve the separation of photogenerated charges. This enhanced separation can be achieved by ferroelectric polarization which allows a very intense modification of the band structure and a much better transport of the photogenerated charges in semiconductors.[46−49] Spontaneous electrical polarization can be obtained through the adjunction of a ferroelectric component to a neighboring semiconductor leading to a significant redistribution of the photogenerated charges and their stabilization at the electrolyte/semiconductor interface.[50] Therefore, locally generating such a polarization by adding a ferroelectric component to a photocatalyst makes it possible to finely adjust the charge separation properties in the semiconductor independently of the potential limitations attributed to the synthesis methods employed. Indeed, a ferroelectric material exhibits a spontaneous polarization due to the displacement of the center of the positive and negative charges in its unit cell. This creates macroscopic charges on the surface of ferroelectrics. Any region with an aligned spontaneous polarization direction is termed a ferroelectric domain. Free electrons will then tend to reach surface positive domains resulting in downward band bending, while on the opposite, positive charges will accumulate on a negative surface domain leading to upward band bending. The resulting separation of charge carriers due to the influence of ferroelectricity on band bending can slow down electron−hole pair recombination in an adjacent semiconductor. Among the possible ferroelectrics, titanates of general formula $ATiO_3$ (with A = Sr, Ba) have interesting ferroelectric properties.

Different methodologies have been considered to build systems combining titanate ferroelectrics and semiconductors[47−52] such as using TiO_2 materials obtained by anodization[51] or rutile nanowires[47,48] followed in all cases by in situ substitution by Sr under hydrothermal conditions. However, even if successful, the results acquired by Zhang et al.[51] but also by Liu et al.[52] were considered as resulting only from a classical heterojunction effect due to the similarity of the band gaps between $SrTiO_3$ and TiO_2.[53] The first attempt considering really the ferroelectric effect was made by Yang et al.[47] by combining a ferroelectric $BaTiO_3$ phase with a TiO_2

https://doi.org/10.1021/acsomega.2c06717
ACS Omega 2023, 8, 8303−8319

semiconductor for photoelectrochemical water splitting application. They were able to determine that a 5 nm $BaTiO_3$-coated TiO_2 rutile nanowire (NW) can achieve an increase of 67% of the photocurrent density compared to TiO_2 NWs alone. Spontaneous polarization of the $BaTiO_3$ film increased the band bending of adjacent TiO_2 NWs slowing down recombination phenomena and therefore increasing the lifetime of photogenerated charges. However, this study suffered from a poor economy of atoms since using massive TiO_2 NWs combined with the least reactive rutile polymorph. Similar conclusions were reached using $SrTiO_3$.[48] Li et al.[54] employed $BaTiO_3$ covered by TiO_2 for photocatalytic hydrogen production but without distinguishing heterojunction effects from ferroelectric polarization. In an interesting study, Huang et al.[49] prepared ferroelectric $BaTiO_3$ NPs combined with CdS and evaluated their photocatalytic efficiency in H_2 production under visible light. A 10-fold increase in H_2 production rate was found when replacing CdS by CdS/$BaTiO_3$. These authors concluded that the ferroelectric polarization of $BaTiO_3$ was the only reasonable explanation for the beneficial effect observed. However, this conclusion was only reached indirectly by default without evidencing clearly the link between polarization and enhanced photocatalytic activity. More recently, Alrashedi et al.[55] showed that the addition of low amounts of strontium onto 0.5 wt % Cu-doped TiO_2 nanotubes (Sr-0.5Cu-TiNT) enhances the photocatalytic degradation of formic acid under UV irradiation. The determination of dielectric properties of Sr-0.5Cu-TiNT strongly emphasizes that an optimum formation of in situ $SrTiO_3$ at the surface of TiO_2 nanotubes helps to stabilize photogenerated charges at the semiconductor surface through in situ polarization effects induced by the ferroelectric domains of the adjacent $SrTiO_3$ species. This effect was related to the metastable paramagnetic nature of $SrTiO_3$, which becomes ferroelectric under small perturbations such as small stress[56] or an electric field.[57] The same authors demonstrated that optimized formation in $SrTiO_3$ was found to be reached at a strontium loading of 0.8 wt % in Sr, while further increase in Sr content to 1.0 wt % leads to the extra formation of SrO species partially covering the Cu-doped TiO_2 nanotubes. This work therefore strongly emphasized the potentiality of using ferroelectric components to induce better stabilized photogenerated charges more available for producing reactive oxygen species (ROS) for photoreaction, even if a direct correlation between photocatalytic activity and polarization had still to be demonstrated.

In the present study, in order to benefit from both a better transfer of charge properties coming from GO and from more stabilized excitons induced by ferroelectrics, graphene oxide was herein combined with ferroelectric Sr- and Cu-doped TiO_2 nanotubes (Sr-Cu-GO-TiNTs) for enhancing the photocatalytic response of the resulting 1D TiO_2 semiconductors. A deep characterization will be devoted to study the structural, textural, morphological, electrical, and dielectric properties of Sr-Cu-GO-NTs nanomaterials. Results of this extensive characterization will then be correlated with an optimized analysis of the kinetic comportment of our photocatalytic systems in order to propose a method allowing one to directly evaluate the potential influence of ferroelectric stabilization of photogenerated charges on the photocatalytic efficiency of an adjacent TiO_2 semiconductor. This study will therefore for the first time propose a direct methodology for correlating detailed kinetic analysis describing photocatalytic properties with dielectric properties and in particular the ability of a given photocatalyst to be polarized.

2. EXPERIMENTAL SECTION

2.1. Elaboration of the Photocatalysts. *2.1.1. Elaboration of TiO_2 Nanotubes.* Titanate nanotubes were synthesized using hydrothermal conditions under strong alkaline concentration as described previously.[19,23,28] A 3 g amount of TiO_2 P25 precursor was first added to 90 mL of a NaOH solution (11.25 mol·L^{-1}) in a 150 mL Teflon-lined autoclave at 130 °C for 20 h (heating ramp, 2 °C/min). Filtration was then performed on the resulting suspension. The as-obtained powder was then contacted to a hydrochloric acid solution (0.1 mol·L^{-1}) before being washed with hot water multiple times to eliminate sodium and chloride. The solution still presenting sodium in excess was then submitted to a subsequent washing with a higher concentrated hydrochloric acid solution (1.0 mol·L^{-1}), leading to complete removal of sodium. The resulting solid was then dried at 80 °C for 12 h. This as-obtained powder was then labeled HTiNT and consists of a hydrogenated $H_2Ti_2O_9·H_2O$ phase.[58] Subsequently, HTiNT was submitted to a calcination treatment under air for 2 h at 400 °C (heating rate, 2 °C/min) to transform the hydrogenotitanate phase into anatase. This sample was then labeled TiNT.

2.1.2. Elaboration of 1 wt % GO-TiO_2 Nanotubes. Graphene oxide-TiNT composite was obtained following an incipient wetness impregnation method of TiNT with 1.0 wt % colloidal solution of graphene oxide (GO).[44] Typically, 1.0 wt % colloidal GO (Sigma-Aldrich, 99.99%, 4 mg·mL^{-1}) was added to TiNT powder and the paste was dried in an oven at 50 °C for 20 h under vacuum. Finally, the material was calcined under air at 400 °C for 2 h (2 °C/min, 60 mL/min). The resulting powder was called GO-TiNT.

2.1.3. Elaboration of Sr-Cu-GO-TiO_2 Nanotubes. First, the GO-TiNT material was doped with an optimum 0.5 wt % copper following an incipient wetness impregnation method as described in earlier work[44] using $Cu(NO_3)_2·3H_2O$ (Sigma-Aldrich, 99%) as precursor. The paste obtained was dried in an oven at 50 °C for 20 h under vacuum and then calcined under air at 400 °C for 2 h (2 °C/min, 60 mL/min). The resulting nanomaterials are named Cu-GO-TiNT. Second, different amounts of strontium (0.2, 0.4, 0.6, 0.8, and 1.0 wt %) were incorporated using a similar incipient wetness impregnation procedure using $Sr(NO_3)_2$ (Sigma-Aldrich, 99.9%) as precursor. Further post-thermal treatment was performed at 400 °C for 2 h using the same procedure as that for copper. Samples were then named as *x*wt%Sr-Cu-GO-TiNT with *x* being the weight percentage in strontium used.

2.2. Catalyst Characterization. A Micromeritics ASAP 2020 apparatus was used to perform N_2 adsorption−desorption measurements at 77 K on the various samples studied here. Specific surface areas were determined, obtained employing the Brunauer−Emmett−Teller (BET) procedure. The relative P/P_0 pressure range extending from 0.05 to 0.25 was chosen while using the experimental values for adsorption. Pore size distributions were determined using the Barrett−Joyner−Halenda (BJH) procedure.

X-ray diffraction (XRD) analysis was performed using an automatic diffractometer (Philips Panalytical X'Pert ProMPD) equipped with a Ni-filtered Cu Kα source. Crystallite sizes were determined using the Scherrer relationship (eq 1).

https://doi.org/10.1021/acsomega.2c06717
ACS Omega 2023, 8, 8303−8319

$$L = K\lambda/\beta \cos\theta \quad (1)$$

with L being the crystallite size, λ the X-ray wavelength (λ = 1.54184 Å), β the full width at half-maximum (fwhm), and K the shape factor (fixed at 1 in this study).

Raman spectroscopy results were performed using a Horiba Jobin Yvon LabRAM-HR apparatus. Spectra were acquired at 20 °C in the wavenumber range extending from 100 to 2500 cm^{-1} (resolution, ±1.5 cm^{-1}). A 514 nm Ar−Kr RM2018 laser was used for excitation, while a CCD detector cooled at −75 °C was employed for the acquisition of the spectra. The power of the Ar−Kr laser was set at 1 mW to hamper any structural modification of the solids during recording.

Scanning electron microscopy (SEM) images with Z-mapping of the $x$wt%Sr-Cu-GO-TiNT solids were studied using an FEI Inspect S50 scanning electron microscope working at 20 kV.

An AvaSpec-2048 fiber optic spectrometer with Czerny−Turner design was employed to acquire UV−vis diffuse reflectance spectra (UV−vis DRS). A 2048 pixel CCD detector was used to determine the optical properties in the 250−800 nm wavelength range. Band gap determination was performed using the Kubelka−Munk procedure. $F(R)h\nu^{1/2}$ vs $h\nu$ plots were obtained with $F(R) = (1 - R)/2R$, considering an indirect transition as expected for TiO_2 anatase.

Dielectric properties were also acquired on the $x$wt%Sr-Cu-GO-TiNT (x = 0.2, 0.4, 0.6, 0.8, and 1) solids as well as on the Sr-free Cu-GO-TiNT given as reference. Herein, samples were investigated as shaped pellets (diameter, 6 mm; thickness, 1 mm) by electrochemical impedance spectroscopy (EIS) using a PalmSens impedance analyzer. All of the measurements were performed over a 1 Hz to 1 MHz frequency range at a voltage amplitude of 0.25 V and over a temperature range comprised between −10 and 60 °C. The temperature was adjusted with a precision of ±1 °C using a recirculating Chiller for the −10 to 10 °C range and using a hot and cold microscope stage for the 20 to 60 °C range. Before conducting the impedance tests, samples were placed between two glasses coated with conductive FTO electrodes. ZView software was utilized to fit the impedance data.

2.3. Photocatalytic Experiments. Photocatalytic reactions were carried out using a 100 mg·L^{-1} formic acid solution (30 mL volume). The test was performed in a 100 mL Pyrex photoreactor equipped with an optical quartz window of 12.5 cm^2 placed above a light source. The photocatalyst concentration was fixed at 1.0 g·L^{-1}, while the pH was maintained at 3.0 ± 0.5. A UV PL-L (18 W) lamp was employed and provided the maximum energy at 365 nm. A Corning filter 0.52 was used to remove wavelength below 340 nm. A 5 mW·min^{-1} flux was set for all measurements. The lamp is turned on 30 min before starting the reaction to stabilize the power of its emission. The suspensions of catalyst and substrate (formic acid) were stirred in the dark for 30 min before the UV irradiation to attain equilibrium for adsorption−desorption. After reaching the adsorption−desorption equilibrium, the FA concentration was set as the initial concentration (C_0). During the UV irradiation, samples were withdrawn from the reactor at constant time intervals (C_t). At the end of the reaction, the catalyst was recovered by simple filtration. A Shimadzu Prominence-i LC-2030C 3D Plus high-performance liquid chromatograph (HPLC) equipped with a Hypersil Gold column (150 mm × 3 mm) and a PDA detector was then used to perform analysis of the samples retrieved from the reactant solution. A water/acetonitrile (45/55) solution was used as a mobile phase flowing at 0.5 mL·min^{-1}.

3. RESULTS AND DISCUSSION

3.1. X-ray Diffraction (XRD). Figure 1A reports the XRD results for the Sr-doped $x$wt%Sr-Cu-GO-TiNT samples (with x = 0.2, 0.4, 0.6, 0.8, and 1.0). For comparison purposes, XRD results obtained for the Sr-free Cu-GO-TiNT and for the Cu-free GO-TiNT were also determined and used as references.

The TiNT exhibited characteristic diffraction peaks at 2θ = 25.4°, 37.8°, 48.1°, 53.9°, 55.0°, and 62.7° ascribed to the (101), (004), (200), (105), (211), and (204) reflection planes of the anatase phase, respectively.[44] Both Cu-GO-TiNT and GO-TiNT (Figure 1B) do not present any shift of the main (101) diffraction peak for anatase, showing that adding copper does not result in any distortion of the bulk TiO_2 lattice as already demonstrated by Reddy et al.[59] Furthermore, the strontium incorporation does not induce either any new XRD signals like those corresponding to SrO. Strontium addition also does not give rise to any shift of the (101) anatase reflection, confirming that the anatase phase is not affected by distortion of the TiO_2 lattice. Considering the differences in radius and charge between Sr^{2+} (1.18 Å) and Ti^{4+} (0.68 Å), this latter result showing that strontium cannot penetrate inside the TiO_2 lattice can be expected. To study the stability of $x$wt%Sr-Cu-GO-TiNT samples, the XRD analysis of the representative 0.8wt%Sr-Cu-GO-TiNT nanocomposite is performed after the photocatalytic test (Figure 1 C). The diffraction peaks of the anatase phase before and after the photocatalytic test are similar and showed no shift of the main (101) diffraction peak for anatase, which confirms the stability of the 0.8wt%Sr-Cu-GO-TiNT nanocomposite.

The Scherrer equation was also utilized (eq 2) to calculate the average size of anatase crystallites:[45]

$$L_{hkl} = \frac{K\lambda}{\beta \cos\left(\frac{2\theta}{2}\right)} \quad (2)$$

with L_{hkl} being the size of the crystallites; K the shape constant; λ the wavelength of the Cu Kα radiation (λ = 1.5406 Å); 2θ the Bragg angle; and β the line width in radians.

The values of anatase crystallite sizes for the $x$wt%Sr-0.5Cu-GO-TiNT materials (with x = 0.2, 0.4, 0.6, 0.8, and 1.0) as well as for the Sr-free Cu-GO-TiNT and for the Cu-free GO-TiNT as references are listed in Table 1. Crystallite sizes are essentially identical for all of the $x$wt%Sr-Cu-GO-TiNT samples (10.7 ± 0.5 nm) and do not differ substantially from the value found for the Cu-GO-TiNT reference (10.2 nm). This last result emphasizes the quite good stabilization of the structural properties of the starting Cu-GO-TiNT solid in accordance with Zghab et al.[44]

3.2. Textural Properties. The textural properties of the $x$wt%Sr-Cu-GO-TiNT materials (with x = 0.2, 0.4, 0.6, 0.8, and 1.0) as well as of the Sr-free Cu-GO-TiNT and the Cu-free GO-TiNT as reference catalysts were examined using N_2 adsorption−desorption measurement at 77 K (Figure 2). The nitrogen adsorption−desorption isotherms present similar profiles whatever the Sr loading with typical type IV curves with H_3 hysteresis loops corresponding to nonrigid aggregates of particles leading to slit-shaped pores. Textural properties are summarized in Table 2. First, the addition of 0.5 wt % Cu leads to a decrease of the BET surface area from 179 to 142 m^2/g. Moreover, with the addition of strontium and up to a loading

https://doi.org/10.1021/acsomega.2c06717
ACS Omega 2023, 8, 8303−8319

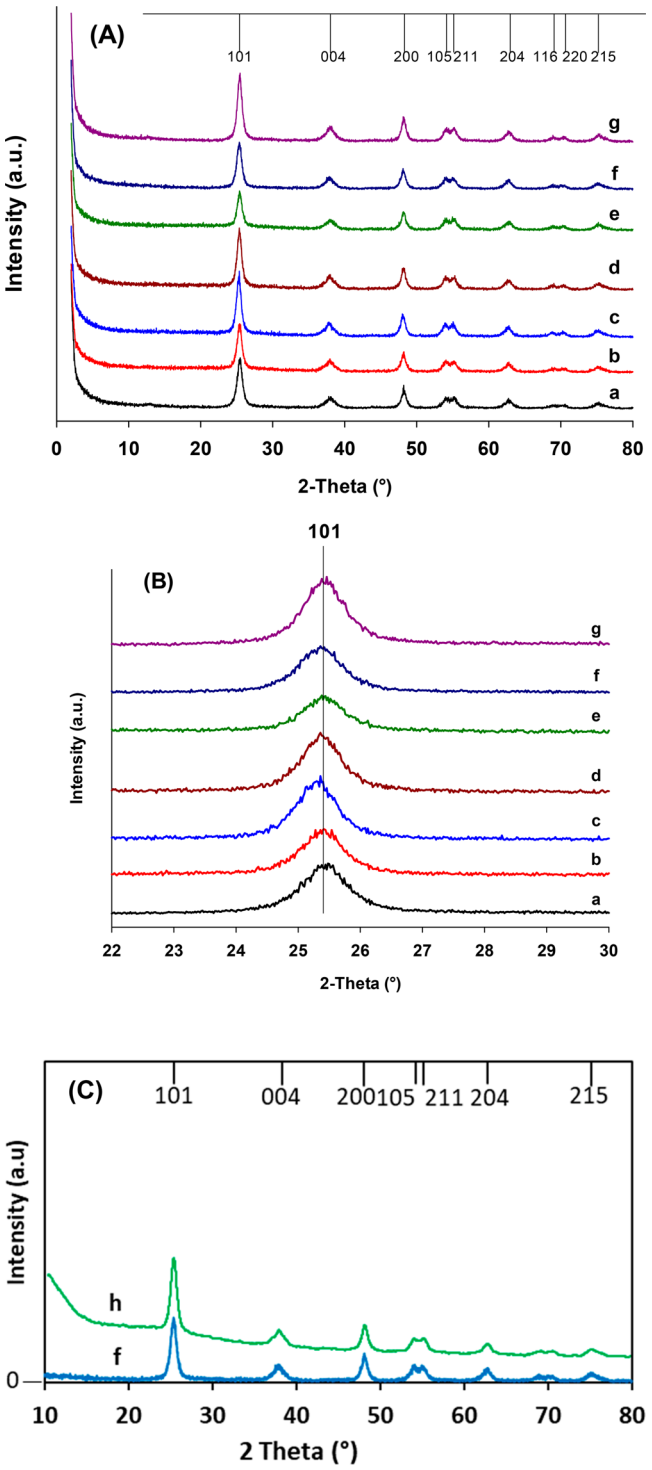

Figure 1. (A) XRD patterns of the *x*wt%Sr-Cu-GO-TiNT nanomaterials with comparison to the copper-free GO-TiNT and the Sr-free Cu-GO-TiNT: (a) GO-TiNT, (b) Cu-GO-TiNT, (c) 0.2wt%Sr-Cu-GO-TiNT, (d) 0.4wt%Sr-Cu-GO-TiNT, (e) 0.6wt%Sr-Cu-GO-TiNT, (f) 0.8wt%Sr-Cu-GO-TiNT, and (g) 1.0wt%Sr-Cu-GO-TiNT. (B) Zoom in of the region of the (101) anatase reflection showing the absence of shift consecutively to the addition of strontium. (C) (f) 0.8wt%Sr-Cu-GO-TiNT, and (h) 0.8wt%Sr-Cu-GO-TiNT after photocatalytic test.

Table 1. Crystallite Sizes Determined by Applying the Scherrer Equation to the (101) Anatase Diffraction Peak and Band Gap Values of GO-TiNT, Cu-GO-TiNT, *x*wt%Sr-Cu-GO-TiNT Nanomaterials, and the 0.8wt%Sr-Cu-GO-TiNT Sample after Photocatalytic Test (Indicated by an Asterisk)

Catalyst	Crystallite Size (nm)	Band Gap (eV)
GO-TiNT	11.7	3.29
Cu-GO-TiNT	10.2	3.26
0.2wt%Sr-Cu-GO-TiNT	10.2	3.27
0.4wt%Sr-Cu-GO-TiNT	10.7	3.27
0.6wt%Sr-Cu-GO-TiNT	10.4	3.27
0.8wt%Sr-Cu-GO-TiNT	10.7	3.26
0.8wt%Sr-Cu-GO-TiNT*	10.6	3.25
1.0wt%Sr-Cu-GO-TiNT	11.1	3.27

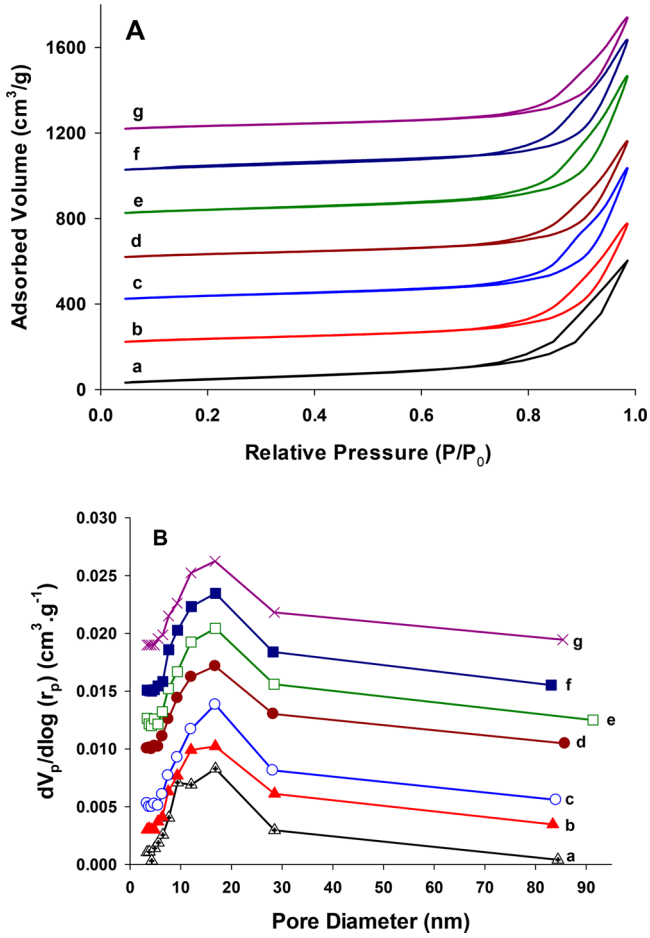

Figure 2. (A) N_2 adsorption−desorption isotherms of the *x*wt%Sr-Cu-GO-TiNT nanomaterials with comparison to the Sr-free Cu-GO-TiNT and (B) BJH pore size distribution plot derived from the desorption branch with (a) GO-TiNT, (b) Cu-GO-TiNT, (c) 0.2wt%Sr-Cu-GO-TiNT, (d) 0.4wt%Sr-Cu-GO-TiNT, (e) 0.6wt%Sr-Cu-GO-TiNT, (f) 0.8wt%Sr-Cu-GO-TiNT, and (g) 1.0wt%Sr-Cu-GO-TiNT.

of 0.8 wt % in Sr, BET specific surface area values vary in a 130−170 m^2/g range without any clear tendency while total pore volumes also vary but in an uncorrelated way with BET surface areas. Finally, average pore diameter values remain constant at about 19 Å. All together, these results suggest that these variations in textural properties mainly result from intergranular porosity between aggregates of bunched TiO_2 nanotubes resulting from van der Waals interactions.[60,61] Strikingly, at the highest Sr loading of 1.0 wt %, a net decrease

https://doi.org/10.1021/acsomega.2c06717
ACS Omega 2023, 8, 8303−8319

Table 2. Textural Properties of Cu-GO-NT and *x*wt%Sr-Cu-GO-TiNT Nanomaterials

Catalyst	BET Surface Area (m^2/g)	Total Pore Vol (cm^3/g)	Av Pore Diam (Å)	N_2 Heat of Adsorption (kJ/mol)
GO-TiNT	179	0.92	20	8.14
Cu-GO-TiNT	142	0.88	19	7.97
0.2wt%Sr-Cu-GO-TiNT	146	0.98	19	7.99
0.4wt%Sr-Cu-GO-TiNT	130	0.86	19	7.82
0.6wt%Sr-Cu-GO-TiNT	155	1.02	19	7.98
0.8wt%Sr-Cu-GO-TiNT	171	0.95	20	7.94
1.0wt%Sr-Cu-GO-TiNT	126	0.83	27	7.89

in surface area to 126 m^2/g (from 171 m^2/g at 0.8 wt % Sr) was observed accompanied symmetrically by a loss of total pore volume to 0.83 cm^3/g and an increase of the average pore diameter to 27 Å. Therefore, in the latter case, the addition of 1.0 wt % Sr starts indicating some degradation of the textural properties of the resulting 1.0wt%Sr-Cu-GO-TiNT material. Determination of N_2 heat of adsorption does not show any variation even at the highest Sr loading of 1.0 wt %, showing that the surface interaction with the adsorbate remains essentially similar whatever the strontium loading.

3.3. Raman Spectroscopy. The *x*wt%Sr-Cu-GO-TiNT nanomaterials were also characterized by Raman spectroscopy (Figure 3). Comparison was also provided to the Sr-free Cu-GO-TiNT solid as a reference. All of the Raman spectra exhibit typical vibration bands expected for the TiO_2 anatase phase with an intense E_{1g} vibration mode at around 145 cm^{-1}. Additional less intense contributions due to anatase can also be noticed at 159 (E_g), 394 (B_{1g}), 514 (B_{1g}/A_{1g}), and 638 cm^{-1} (E_g).[9] Moreover, no new vibration bands due to copper or strontium can be noticed, confirming previous XRD observations about the very high degree of Cu and Sr dispersion achieved on these materials.

A deeper analysis of the main E_{1g} vibration mode reveals some significant shifts with increasing Sr loading with blue and red shifts observed at Sr content similar to that in our previous study on GO-free Sr-Cu-TiNT solids.[55] In this respect, the addition of 0.2 wt % Sr leads to a blue shift of the main E_{1g} vibration mode from 145.3 to 145.8 cm^{-1}. This blue shift is attributed to the creation of surface oxygen vacancies[62] directly resulting from the implementation of strontium onto the surface of TiO_2 nanotubes. As soon as a Sr loading of 0.4 wt % is reached, an opposite shift to lower values is observed. This red shift leads to maxima for the E_{1g} vibration mode, moving from 145.8 cm^{-1} for 0.2wt%Sr-Cu-GO-TiNT to 145.6 cm^{-1} for 0.4wt%Sr-Cu-GO-TiNT, 145.3 cm^{-1} for 0.6wt%Sr-Cu-GO-TiNT, and finally 145.2 cm^{-1} for 0.8wt%Sr-Cu-GO-TiNT. The reasons behind such a red shift can be multiple: crystalline lattice distortion of the anatase phase,[63] heterogeneous particle size distribution,[64] or formation of a new phase at the surface of the nanotubular structure.[65] Previous XRD results have been demonstrated that such a shift cannot be attributed to lattice distortion of the anatase phase. Similarly, at such low loadings of strontium deposited onto a high surface area titanium oxide, it is quite improbable that non-uniform distribution would be achieved. The absence of Sr signals on Raman spectra supports this assumption. The red shift can then be attributed to the formation of a new phase ($SrTiO_3$ or SrO) on the surface of the TiO_2 nanotubes. The creation of surface oxygen vacancies at a very low loading in strontium of 0.2 wt % results from a strong initial interaction between strontium and titania inducing the creation of $SrTiO_3$ entities on the semiconductor surface as already observed on GO-free Sr-Cu-TiNT solids.[55] The similar shift variations observed here at a given Sr loading whatever the presence of GO reflect the absence of perturbation coming from graphene oxide and susceptible to influencing the Sr-TiO_2 interaction. Increasing further the Sr loading to 1.0 wt % leads to a new significant blue shift of the E_{1g} vibration mode from 145.2 to 146.0 cm^{-1}, suggesting the formation of segregated SrO-like species at excess Sr loadings. Finally, some variations in intensity of the E_{1g} mode of vibration can be noticed, suggesting some heterogeneity in terms of crystallinity of the TiO_2 anatase phase.

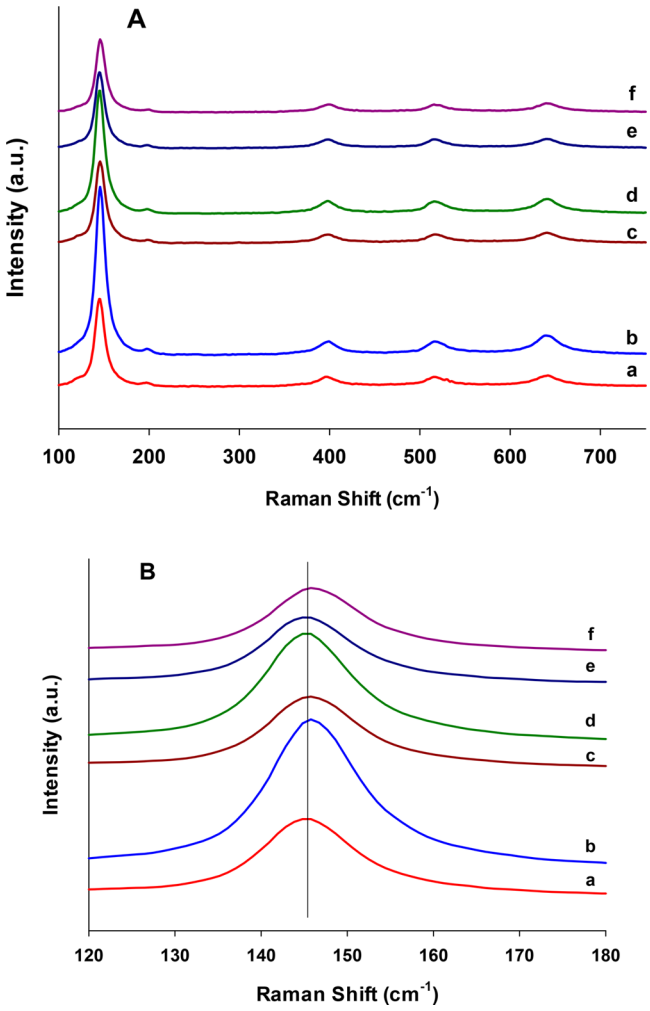

Figure 3. (A) Raman spectra of the *x*wt%Sr-Cu-GO-TiNT materials: (a) Cu-GO-TiNT, (b) 0.2wt%Sr-Cu-GO-TiNT, (c) 0.4wt%Sr-Cu-GO-TiNT, (d) 0.6wt%Sr-Cu-GO-TiNT, (e) 0.8wt%Sr-Cu-GO-TiNT, and (f) 1.0wt%Sr-Cu-GO-TiNT. (B) Zoom in to the region of the E_{1g} active mode of anatase showing the presence of shift effects with the addition of strontium.

3.4. UV−Vis Diffuse Reflectance Spectroscopy. UV−vis diffuse reflectance spectra (DRS) of the *x*wt%Sr-Cu-GO-TiNT materials with Sr loading ranging from 0.2 to 1.0 wt % are reported in Figure 4. Comparison is provided to TiNT alone, the GO-TiNT sample, and the Sr-free Cu-GO-TiNT solid. All materials exhibit a strong absorption up to 350 nm corresponding to O^{2-} (2p) → Ti^{4+} (3d) charge transfer bands.[38] However, the addition of graphene oxide leads to a

https://doi.org/10.1021/acsomega.2c06717
ACS Omega 2023, 8, 8303−8319

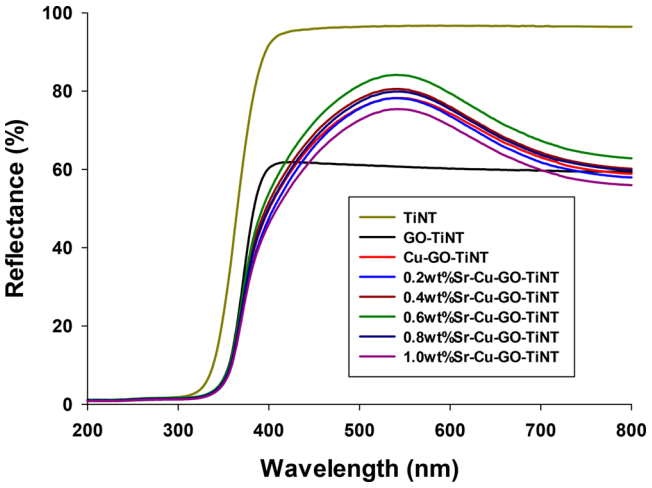

Figure 4. UV−vis diffuse reflectance spectra of the *x*wt%Sr-Cu-GO-TiNT materials with comparison to TiNT, GO-TiNT, and Cu-GO-TiNT: (a) TiNT, (b) GO-TiNT, (c) Cu-GO-TiNT, (d) 0.2wt%Sr-Cu-GO-TiNT, (e) 0.4wt%Sr-Cu-GO-TiNT, (f) 0.6wt%Sr-Cu-GO-TiNT, (g) 0.8wt%Sr-Cu-GO-TiNT, and (h) 1.0wt%Sr-Cu-GO-TiNT.

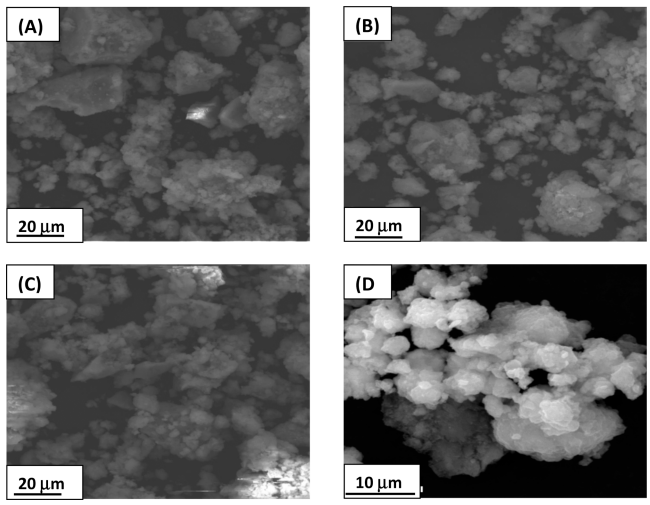

Figure 5. SEM images of (A) Cu-GO-TiNT, (B) 0.4wt%Sr-Cu-GO-TiNT, (C) 0.6wt%Sr-Cu-GO-TiN,T and (D) 0.8wt%Sr-Cu-GO-TiNT.

small shift of the onset value for this absorption band to higher wavelength. Band gap values using the Kubelka−Munk method were then determined assuming an indirect transition as expected for anatase. Results first confirm that the GO addition leads to a slight decrease of the E_g value from 3.47 eV for TiO_2 nanotubes to 3.29 eV for GO-TiNT (Table 1). This slight decrease of the band gap energy results either from surface states or impurity energy bands due to the interaction between TiO_2 nanotubes and GO[66] or from the formation of Ti−O−C chemical bonds.[67,68] The addition of 0.5 wt % Cu does not modify the band gap energy values (3.26 eV), confirming previous observations about the absence of incorporation of copper inside the TiO_2 matrix.[44] However, copper addition also leads to the appearance of two new contributions around 420 and 800 nm whose intensities remains constant afterward with the introduction of strontium. The 420 nm signal is assigned to Cu(I) oxide entities either like Cu^+ 3D clusters in CuO matrix[69,70] or as separate Cu_2O species.[38,71,72] The second contribution around 800 nm is assigned to octahedral Cu^{2+} species ($^2E_g \rightarrow {}^2T_{2g}$ d−d transition).[73,74]

Further addition of strontium up to 1.0 wt % does not modify the UV−vis DRS profiles with similar onset values for the main absorption band and therefore similar energy band gap values (3.26−3.27 eV). This result confirms our previous XRD observations about the fact that strontium is not incorporated inside the TiO_2 matrix.

3.5. SEM-EDX Analysis. The morphological analysis of the *x*wt%Sr-Cu-GO-TiNT materials and of the Cu-GO-TiNT reference was performed using scanning electron microscopy (SEM) (Figure 5).

SEM images reveal that essentially identical morphologies were observed for all the Sr-containing samples with rough aggregates forming intergranular pores. This agrees with the fact that strontium does not alter the aggregation degree of the *x*wt%Sr-Cu-GO-TiNT samples.

EDX analysis was also performed to ascertain the surface distribution of the Cu-GO-TiNT reference and of the 0.4wt% Sr-Cu-GO-TiNT sample (Supporting Information Figure S1), while *Z*-elemental mappings were also obtained (Figure 6). The EDX analysis of 0.6wt%Sr-Cu-GO-TiNT and 0.8wt%Sr-Cu-GO-TiNT (before and after photocatalytic testing) as well as their corresponding *Z*-mappings are given in Supporting Information (Figures S2 and S3). Cu, Ti, C, and O elements were detected by EDX analysis onto Cu-GO-TiNT, while Sr was also found onto 0.4wt%Sr-Cu-GO-TiNT. A more in-depth examination of these elements in three different areas shows a quite homogeneous distribution.

The corresponding elemental mapping images of Cu-GO-TiNT (Figure 6A) and of 0.4wt%Sr-Cu-GO-TiNT (Figure 6B) show a quite good homogeneous dispersion of copper and strontium in agreement with the conclusion reached using X-ray diffraction. Finally, EDX analysis of 0.8wt%Sr-Cu-GO-TiNT (Figure S2B) and of 0.8wt%Sr-Cu-GO-TiNT after photocatalytic testing (Figure S2C) shows a quite good homogeneous dispersion. The average molar ratios of Sr/Ti, and Cu/Ti are respectively 0.028 and 0.034 against 0.020 and 0.030 after the photocatalytic testing, which confirms the stability of the Sr-Cu-GO-TiNT nanocomposites.

3.6. Photoluminescence Spectroscopy. Figure 7 shows the photoluminescence (PL) spectra of TiNT alone, GO-TiNT, and Cu-GO-TiNT in the 350−620 nm wavelength range. Photoluminescence spectroscopy gives information on the recombination and migration of photogenerated electron−hole pairs. To study the luminescent defect state of the prepared samples, radiation at a wavelength of 350 nm as excitation was used. One should note that PL spectra generally result from several emission peaks corresponding to (1) phonon-assisted indirect transition from the edge (χ) to the center (Γ) of the Brillouin zone at about 380 nm;[23,75] (2) charge transfer contributions from Ti^{3+} species to TiO_6^{2-} octahedra around 490 nm,[76] hardly detectable here and showing a low Ti^{3+} contribution in agreement with our previous investigation on Sr-Cu-TiNT materials;[55] (3) around 450 nm, bulk recombination processes between self-trapped electrons and holes;[77,78] and (4) recombination of electrons with surface oxygen defects[78] at around 465 and 560 nm. The addition of graphene oxide to the TiNT material results in a modification of the PL profile. However, variation in PL absolute intensity cannot be analyzed in the present case as simply reflecting changes in recombination processes since graphene oxide was already found to shield PL contributions

https://doi.org/10.1021/acsomega.2c06717
ACS Omega 2023, 8, 8303−8319

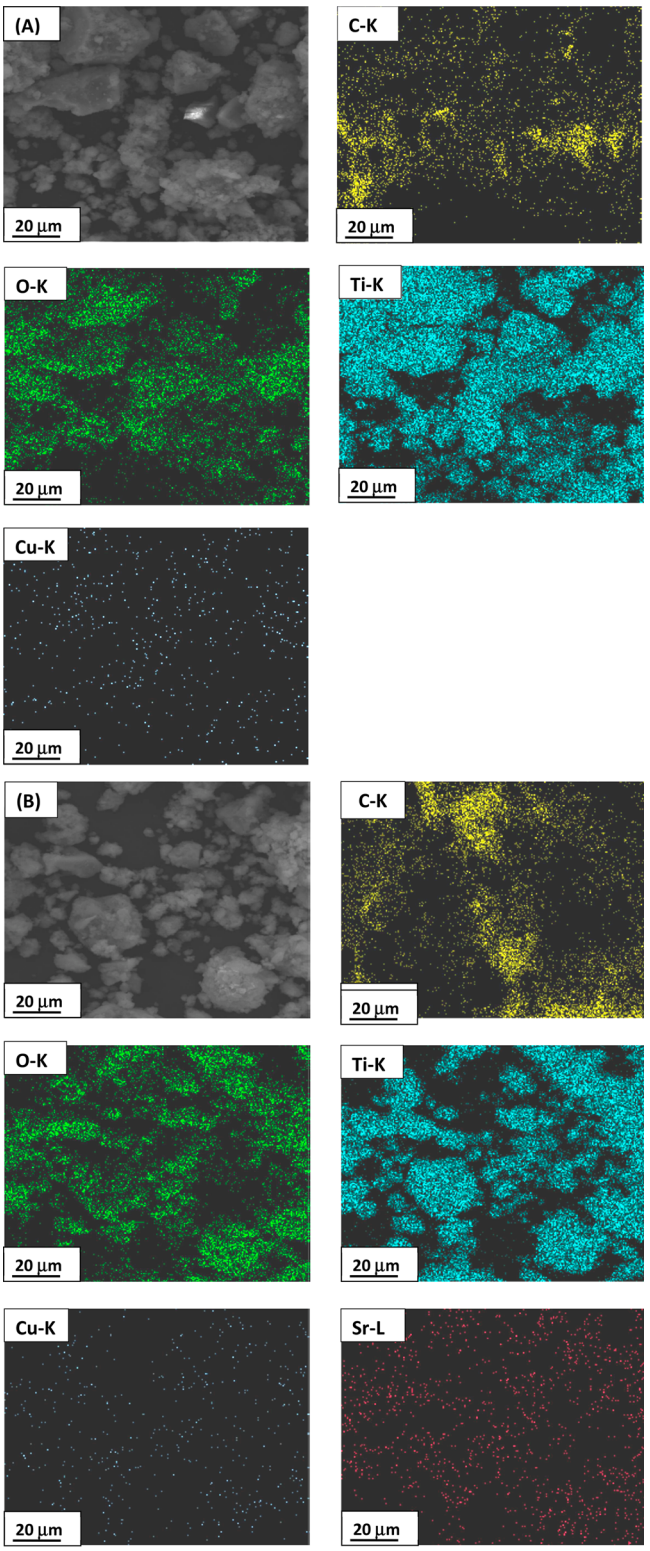

Figure 6. EDX mapping analysis of (A) Cu-GO-TiNT (given as reference) and (B) 0.4wt%Sr-Cu-GO-TiNT.

from the TiO_2 semiconductor since GO is expected to partly wrap the nanotube surface.[79] Nevertheless, independently of the shielding effect due to GO, relative respective contributions from each emission peak can still be determined, showing, on GO-TiNT, a relatively lower contribution around 450 nm corresponding to a lower proportion of bulk recombination of

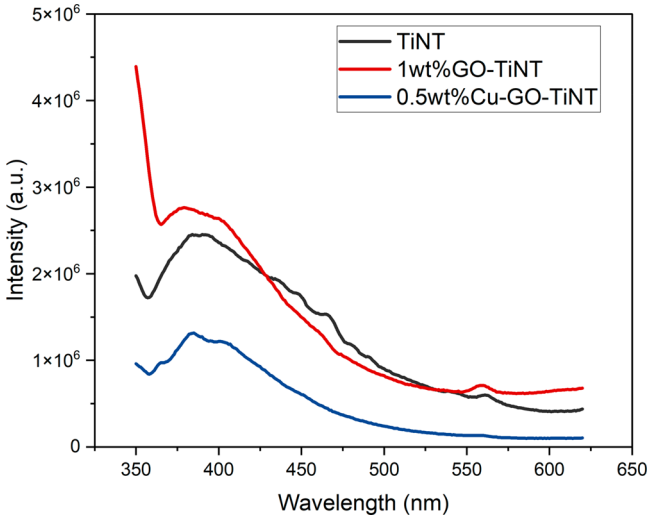

Figure 7. Photoluminescence spectra of TiNT, GO-TiNT, and Cu-GO-TiNT used as references.

electron−hole pairs in agreement with our preceding study on GO-TiNT systems.[79]

The addition of 0.5 wt % Cu to the GO-TiNT material results in a significant loss of PL intensity, showing a strong decrease of the different processes leading to photoluminescence signals on our curves with an even slightly more marked decline in intensity around 450 nm, suggesting lower electron−hole recombination processes particularly for self-trapped electrons in the bulk.

Figure 8 reports the PL spectra of the Cu-GO-TiNT samples after incorporation of various amounts of strontium (from 0.2

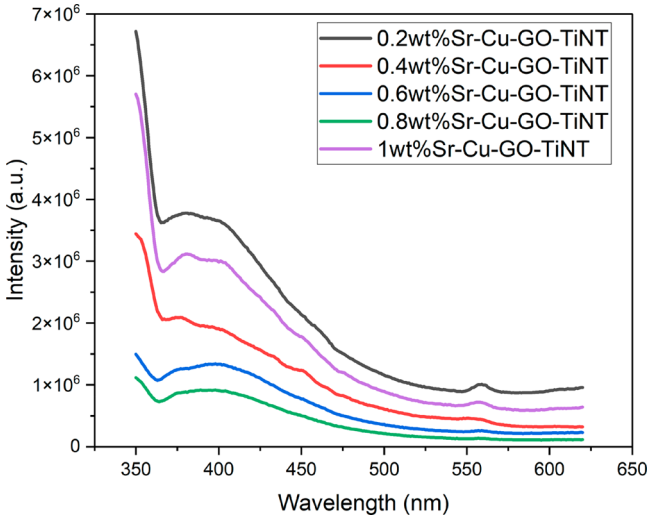

Figure 8. Photoluminescence spectra of the *x*wt%Sr-Cu-GO-TiNT materials with *x* varying between 0.2 and 1.0 wt % Sr.

to 1.0 wt %). The addition of strontium results in a strong decrease of the PL intensity up to 0.8 wt % Sr loading with a signal four times lower for 0.8wt%Sr-Cu-GO-TiNT than for 0.2wt%Sr-Cu-GO-TiNT.

This general decrease in intensity is however not associated with changes in the respective contributions of the different emission peaks. This result agrees with previous observations on GO-free Sr-Cu-TiNT materials[55] showing a lower tendency

https://doi.org/10.1021/acsomega.2c06717
ACS Omega 2023, 8, 8303−8319

Table 3. Kinetic Parameters Determined Assuming Either a Pseudo-First-Order or a Pseudo-Second-Order Kinetics Law for the *x*wt%Sr-Cu-GO-TiNT Materials (with *x* Varying between 0.2 and 1.0 wt %) with Comparison to the Sr-Free Cu-GO-TiNT Reference

		Pseudo-First-Order		Pseudo-Second-Order	
Sr Content (wt %)	Catalyst	k_1 (min^{-1})	R^2	k_2 ($mol^{-1}·L·min^{-1}$)	R^2
0	Cu-GO-TiNT	0.0304	0.9566	0.0075	0.9920
0.2	0.2wt%Sr-Cu-GO-TiNT	0.0336	0.9934	0.0168	0.9763
0.4	0.4wt%Sr-Cu-GO-TiNT	0.0443	0.9974	0.0248	0.9900
0.6	0.6wt%Sr-Cu-GO-TiNT	0.0388	0.9840	0.0158	0.9431
0.8	0.8wt%Sr-Cu-GO-TiNT	0.0340	0.9919	0.0356	0.9702
1.0	1.0wt%Sr-Cu-GO-TiNT	0.0370	0.9993	0.0168	0.9763

for recombination either in the bulk or with surface oxygen vacancies. Therefore, the addition of strontium up to 0.8 wt % leads undoubtedly to a lower propensity for recombination. Moreover, this lower tendency for recombination is not linked to any change in structural properties able to induce variations in the optical response. The situation becomes strikingly different when further increasing the Sr content to 1.0 wt % with a sudden strong re-increase of the PL intensity, demonstrating in this case a rise in the ability for recombination processes when strontium is added in excess. This last result confirms a change in structural properties as observed previously and resulting probably from the formation of segregated SrO species.

3.7. Evaluation of the Photocatalytic Properties. *3.7.1. Kinetic Study of The Photodegradation of Formic acid.* The influence of strontium on the photocatalytic performance of *x*wt%Sr-Cu-GO-TiNT materials was then evaluated considering formic acid (FA) as a representative example of many organic pollutants containing carboxylic functions. FA is also a molecule of choice for photocatalytic evaluation since it represents very often the last intermediate before complete mineralization into CO_2.

FA photodegradation was performed under UV-A irradiation for the series of *x*wt%Sr-Cu-GO-TiNT materials (with *x* varying between 0.2 and 1.0) by comparison to the Cu-GO-TiNT reference. The first initial step in our kinetic analysis was to determine the order of the reaction for FA photodegradation. In this respect, the general kinetic equation for the FA photodegradation rate is expressed in eq 3:

$$\text{rate} = -\frac{\mathrm{d[FA]}}{\mathrm{d}t} = k_i[\mathrm{FA}]^{\alpha} \quad \text{(at constant temperature)} \tag{3}$$

Assuming that the FA degradation rate follows a pseudo-first-order kinetics, then $\alpha = 1$ and eq 3 becomes

$$\text{rate} = -\frac{\mathrm{d[FA]}}{\mathrm{d}t} = k_i[\mathrm{FA}] \tag{4}$$

$$\frac{\mathrm{d[FA]}}{\mathrm{[FA]}} = -k_1\,\mathrm{d}t \tag{5}$$

Integrating eq 5 from the initial concentration at $t = 0$ to the final concentration at t (>0) results in eq 6:

$$\ln\left(\frac{C_t}{C_0}\right) = -k_1 t \tag{6}$$

with $[\mathrm{FA}]_0 = C_0$ being the initial FA concentration and $[\mathrm{FA}]_t = C_t$ the FA concentration at time t.

Similarly, if the reaction follows a pseudo-second-order kinetics ($\alpha = 2$), eq 7 is obtained:

$$\frac{1}{[\mathrm{c}]_t} = \frac{1}{[\mathrm{c}]_0} + k_2 t \tag{7}$$

Plotting $\ln\left(\frac{[\mathrm{c}]_t}{[\mathrm{c}]_0}\right)$ or $\frac{1}{[\mathrm{c}]_t}$ vs t can therefore help to determine if the photodegradation reaction follows a first- or second-order kinetics.

Values for the respective pseudo-first-order rate constant values (k_1) or -second-order rate constant values (k_2) are given in Table 3.

Comparison reported in Table 3 between pseudo-first-order or -second-order kinetic models clearly underlines a better fit of the kinetic results assuming a pseudo-first-order model. In this respect, compared to the Sr-free Cu-GO-TiNT, the addition of 0.2 wt % Sr already increases the rate constant value k_1 by 11%, while an optimum is reached at 0.4 wt % Sr with a rate constant 46% higher than for the Sr-free counterpart. Comparison between Cu-TiNT (k = 64 $\mu mol·L^{-1}·min^{-1}$),[55] 0.8wt%Sr-Cu−TiNT (k = 88 $\mu mol·L^{-1}·min^{-1}$),[55] and 0.8wt%Sr-Cu-GO-TiNT (k = 103 $\mu mol·L^{-1}·min^{-1}$) (this work) shows a beneficial influence of the presence of GO on the photocatalytic response. The maximum k value observed at 0.8wt%Sr-Cu-GO-TiNT is here 37% higher than for 0.8wt%Sr-Cu-TiNT and 61% higher than for Cu-TiNT. As highlighted in the next section about dielectric properties, the enhancement observed due to the addition of strontium to Cu-GO-TiNT is related to the creation of highly polarized system allowing a better separation of photogenerated electron−hole pairs.

The analysis of Table 3 and of the resulting R^2 values obtained by considering a pseudo-first-order model, even if apparently satisfying, shows some slight but significant divergence from linearity particularly for the Sr-free Cu-GO-TiNT and the 0.6wt%Sr-Cu-GO-TiNT samples and to a lesser extent for 0.8wt%Sr-Cu-GO-TiNT. Therefore, and to deepen our analysis of our kinetic results, a procedure using an ideal pseudo-average-order k_n ($n > 1$ and $n \neq 1$) was used to correlate our photodegradation reaction as expressed in eq 8:

$$\frac{C}{C_0} = [(n-1)k_n t + 1]^{-1/(n-1)} \tag{8}$$

A nonlinear regression used to determine the resulting pseudo-order value was then applied giving rise to a value for n of 1.9. Figure 9 exemplifies the resulting variation of the predicted C/C_0 ratio obtained for this model vs experimental C/C_0 values in the case of the 0.4wt%Sr-Cu-GO-TiNT material (k_n = 0.075 min^{-1} and n = 1.9). Results emphasize a good correlation

https://doi.org/10.1021/acsomega.2c06717
ACS Omega 2023, 8, 8303−8319

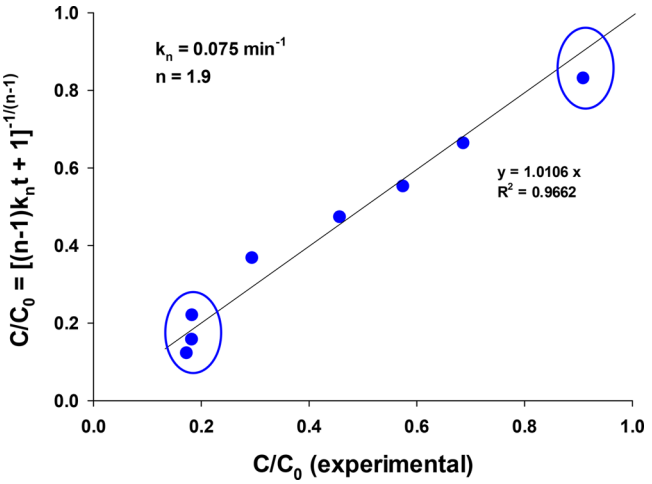

Figure 9. Correlation between predicted C/C_0 obtained by the nonlinear regression model (with k_n = 0.075 min^{-1} and n = 1.9) vs experimental C/C_0 values in the case of the 0.4wt%Sr-Cu-GO-TiNT material.

between predicted and experimental C/C_0 ratios with a resulting slope only slightly deviating from unity (1.0106) and a R^2 value of 0.9662. However, some significant deviations from this model can still be observed at low and high conversion as encircled in Figure 9. This kinetic model was then applied to all of the *x*wt%Sr-Cu-GO-TiNT materials, and results are summarized in Table 4.

Table 4. Kinetic Parameters As Determined by Applying a Nonlinear Regression of the $\frac{C}{C_0} = [(n-1)k_n t + 1]^{-1/(n-1)}$ Kinetics Law (n = 1.9) for the Series of *x*wt%Sr-Cu-GO-TiNT Materials[a]

Catalyst	k_n (min^{-1})	R^2
Cu-GO-TiNT	0.042	0.9906
0.2wt%Sr-Cu-GO-TiNT	0.066	0.9870
0.4wt%Sr-Cu-GO-TiNT	0.075	0.9906
0.6wt%Sr-Cu-GO-TiNT	0.066	0.9925
0.8wt%Sr-Cu-GO-TiNT	0.062	0.9888
1.0wt%Sr-Cu-GO-TiNT	0.060	0.9912

[a]Comparison is provided with the Cu-GO-TiNT reference.

The substantial deviations observed in Figure 9, as well as the limited range of C/C_0 values for which this modified model applies, significantly impacts the precision of the n value. In order to restrain divergence between experimental and calculated values, the pseudo-first-order model as shown in eq 6 has been extended to integrate a second component, turning it into a second-degree polynomial through the addition of a t^2 term as expressed in eq 9.

$$\ln\left(\frac{C}{C_0}\right) = -a_1 t + a_2 t^2 \quad (9)$$

The parameter a_1 can be transformed into a common factor (eq 10) equivalent to a kinetic rate constant. This modification helps to compare in a more straightforward way the pseudo-first-order results (eq 6) with those obtained using the present proposed modified model (eq 10):

$$\ln\left(\frac{C}{C_0}\right) = -a_1 t(1 - \alpha t) \quad (10)$$

The resulting new kinetic parameters and the correlation coefficients R^2 are reported in Table 5, while Figure 10 exhibits the correlation between the $\ln\left(\frac{C}{C_0}\right)$ term from the modified kinetic model and the experimental values in the case of the 0.4wt%Sr-Cu-GO-TiNT sample.

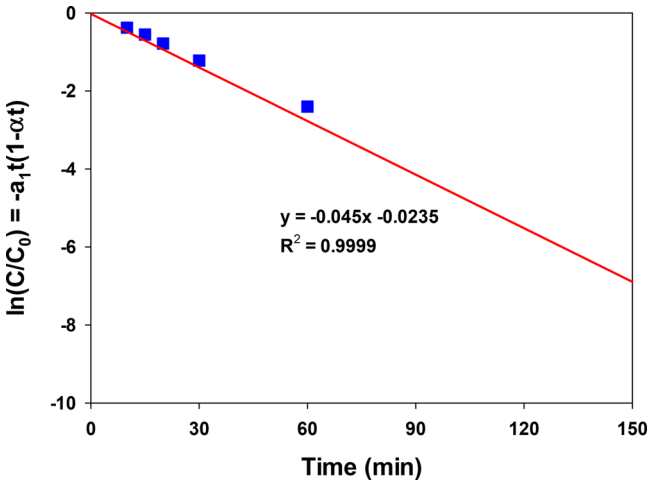

Figure 10. Variation of $\ln\left(\frac{C}{C_0}\right) = -a_1 t(1 - \alpha t)$ vs time for the 0.4wt%Sr-Cu-GO-TiNT material (a_1 = 0.04 min^{-1} and $\alpha = 1.50 \times 10^{-4}$ min^{-1}): red line (model) and blue squares (experiments).

Figure 10 shows that the values of $\ln\left(\frac{C}{C_0}\right)$ obtained from the modified kinetic model fit well with the experimental results.

Table 5. Kinetic Parameters Obtained from the Modified Kinetic Model ($\ln\left(\frac{C}{C_0}\right) = -a_1 t(1 - \alpha t)$) and from the Intradiffusion Model ($\ln\left(\frac{C}{C_0}\right) = -k_d\sqrt{t}$) (with $\tau_d = \frac{1}{k_d^2}$) for the Series of *x*wt%Sr-Cu-GO-TiNT Materials[a]

wt % Sr	a_1 (min^{-1})	a_2 (min^{-2})	α (min^{-1})	R^2	k_d ($min^{-0.5}$)	R^2	τ_d (min)
0	0.033	3.9×10^{-7}	1.2×10^{-5}	0.9999	0.37	0.9848	7.3
0.2	0.041	6.2×10^{-6}	1.5×10^{-4}	0.9999	0.26	0.9606	15.1
0.4	0.046	6.9×10^{-6}	1.5×10^{-4}	0.9999	0.27	0.9845	13.7
0.6	0.040	6.0×10^{-6}	1.5×10^{-4}	0.9999	0.24	0.9832	17.5
0.8	0.036	5.4×10^{-6}	1.5×10^{-4}	0.9999	0.23	0.9783	18.9
1.0	0.035	5.2×10^{-6}	1.5×10^{-4}	0.9999	0.25	0.9751	16.4

[a]Comparison is provided with the Sr-free Cu-GO-TiNT reference.

https://doi.org/10.1021/acsomega.2c06717
ACS Omega 2023, 8, 8303−8319

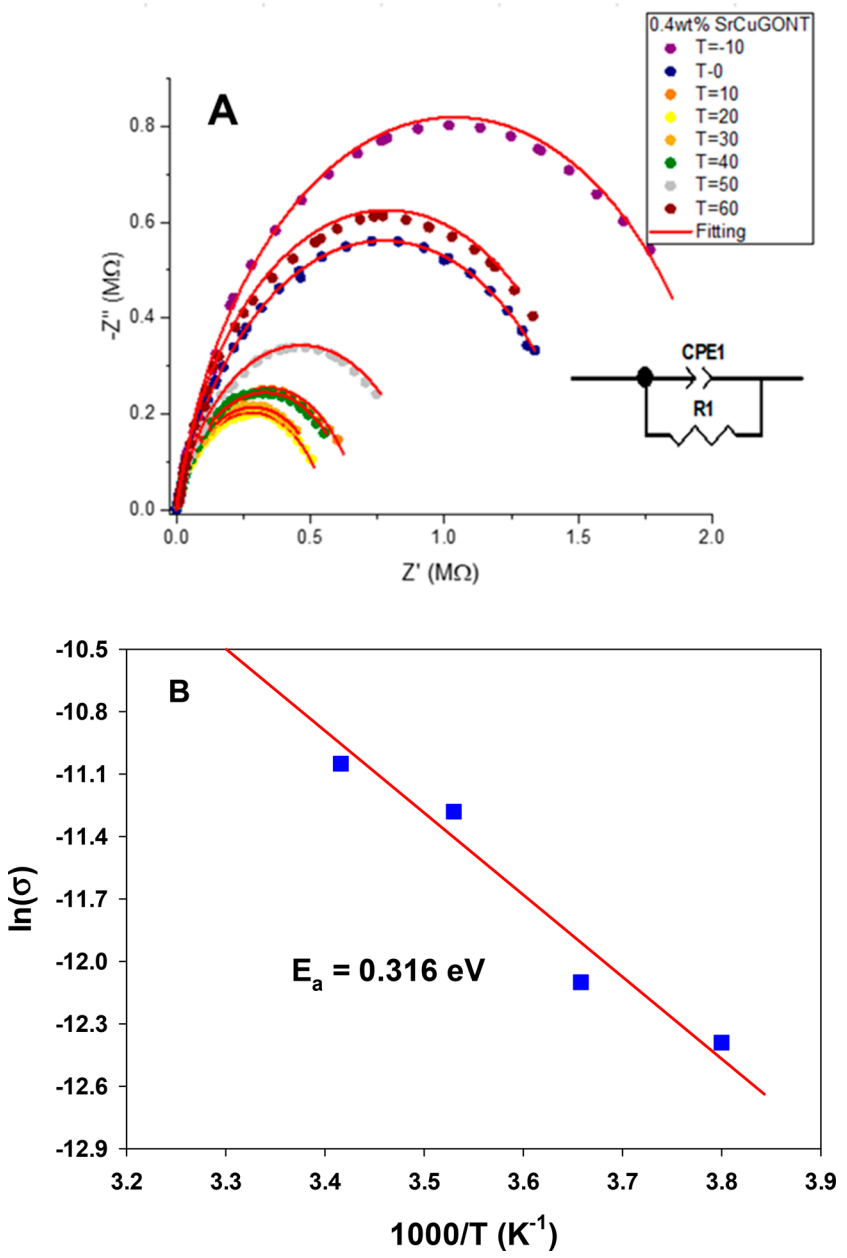

Figure 11. (A) Nyquist diagrams acquired for the 0.4wt%Sr-Cu-GO-TiNT sample at temperatures of acquisition varying between −10 °C and +60 °C with corresponding fitting simulations and representation of the equivalent electric circuit and (B) Arrhenius plot of $\ln(\sigma T)$ vs $1000/T$.

Table 5 reports the values obtained for the kinetic parameters a_1, a_2, and α as well as the correlation coefficients R^2 for all of the Sr-containing samples with comparison to the Sr-free reference. In all cases, the correlation coefficient R^2 is quite close to unity, emphasizing a quite good fit, much better than that with the unmodified first-order kinetic model (cf. Table 3). Compared to the Sr-free reference, the kinetic parameter a_1 increases by a factor of 25% for 0.2wt%Sr-Cu-GO-TiNT, while an increase by 40% is observed at the optimum for the 0.4wt% Sr-Cu-GO-TiNT sample. At higher Sr loading, the beneficial effect due to the addition of strontium declines going back for 0.6wt%Sr-Cu-GO-TiNT to a value similar to the 0.2wt%Sr-Cu-GO-TiNT sample, while almost any beneficial effect due to strontium is lost for 1.0wt%Sr-Cu-GO-TiNT.

3.7.2. Intradiffusion Kinetic Analysis. The preceding modified kinetic model by fitting almost perfectly experimental values through the addition of a second polynomial term to the initial pseudo-first-order model reflects the influence of intradiffusion phenomenon influencing the kinetic response of the Sr-containing Cu-GO-TiNT materials. To better ascertain this phenomenon, an intradiffusion study was therefore performed. In this respect, a kinetic law considering a k_d intradiffusion rate was considered (eq 11).

$$\ln\left(\frac{C}{C_0}\right) = -k_d\sqrt{t} \tag{11}$$

Results about fitting using the intradiffusion rate law were therefore obtained, and the resulting values are reported in Table 5. Even if the correlation coefficients R^2 differ from unity, a quasi-linearity can still be found with R^2 values ranging between 0.960 and 0.985.

From Table 5, one should observe the influence of the intradiffusion phenomenon which results in a decrease by 30%

https://doi.org/10.1021/acsomega.2c06717
ACS Omega 2023, 8, 8303−8319

Table 6. Fitting Simulation Results of the Nyquist Curves for the Series of *x*wt%Sr-Cu-GO-TiNT Samples with $0 \leq x \leq 1$ (*R*, Resistance; *C*, Capacitance; *n*, Dimensionless Parameter Describing Deviation from an Exact Semicircle; E_a, Activation Energy)

wt % Sr	Catalyst	*R* (MΩ)	*C* (10^{-11} F)	*n*	τ (μs)	E_a (eV)
0	Cu-GO-TiNT	1.18	1.90	0.81	2.24	0.044
0.2	0.2wt%Sr-Cu-GO-TiNT	1.48	1.44	0.81	2.13	0.160
0.4	0.4wt%Sr-Cu-GO-TiNT	5.17	9.34	0.87	48.3	0.316
0.6	0.6wt%Sr-Cu-GO-TiNT	1.10	9.87	0.86	10.9	0.270
0.8	0.8wt%Sr-Cu-GO-TiNT	3.54	1.24	0.85	4.4	0.407
1.0	1.0wt%Sr-Cu-GO-TiNT	3.61	1.55	0.81	5.6	0.470

of the intradiffusion rate k_d upon addition of low strontium loading as soon as 0.2 wt %. For all Sr-containing photocatalysts, the intradiffusion rate k_d value remains relatively similar with an average value of 0.25 $min^{-0.5}$ with a standard deviation of only 0.015 $min^{-0.5}$. Equation 11 can also be reformulated as expressed in eq 12.

$$\ln\left(\frac{C}{C_0}\right) = -\sqrt{\frac{t}{\tau_d}} \tag{12}$$

with $\tau_d = \frac{1}{k_d^2}$ being the parameter which indicates the intradiffusion specific time.

The different τ_d values for the series of Sr-containing Cu-GO-TiNT samples are reported in Table 5. The Sr-free Cu-GO-TiNT solid shows the lowest τ_d value. The intradiffusion phenomenon therefore plays a more important role for this latter sample than for the Sr-containing Cu-GO-TiNT solids. The highest τ_d value is achieved for the 0.8wt%Sr-Cu-GO-TiNT sample.

3.8. Determination of Dielectric Properties by Electrochemical Impedance Spectroscopy. *3.8.1. Analysis of Nyquist Curves.* Electrochemical impedance spectroscopy (EIS) analysis was performed for the Sr-containing Cu-GO-TiNT samples as well as for the Sr-free Cu-GO-TiNT reference in order to determine the evolution of the dielectric properties of copper-doped GO-NT solids when strontium was progressively added to the different photocatalytic systems. In this respect, as an example, Figure 11A reports the Nyquist diagram achieved for the 0.4wt%Sr-Cu-GO-TiNT sample at different temperatures of acquisition ranging from −10 to +60 °C. Similarly, Nyquist curves were also acquired in the same temperature range of acquisition for the other samples of the *x*wt%Sr-Cu-GO-TiNT series (with $0 \leq x \leq 1$) and results are reported in Figure S4.

As shown in Figure 11A, scattered experimental values ($-Z''$ vs Z') are roughly distributed on a circular arc. This is generally related to an electric dipole composed of a resistance in parallel with a capacitor. This approach is however sometimes oversimplistic because the scattered points are not always distributed perfectly on half-circles. Therefore, combining a resistance with a capacitor in parallel is sometimes a too approximate way to represent the EIS results. A constant phase element (CPE) in parallel with a resistance is often a better approach to describe the parameters fitting the equivalent circuits.[80] The equivalent electrical circuit of the samples is shown in the inset of Figure 11A. The best fitting simulations of the experimental results are given in red lines.

The total impedance of the circuit is given in eq 13:

$$Z^* = \mathrm{Re}Z^* + \mathrm{Im}Z^* = Z' + jZ'' = \left(\frac{1}{R} + \frac{1}{Z^*_{CPE}}\right) \tag{13}$$

with the impedance of the CPE component defined via[81]

$$Z^*_{CPE} = \frac{1}{A_0(j\omega)^n} \tag{14}$$

with ω being the angular frequency ($\omega = 2\pi f$) and A_0 a constant independent of frequency[80], while *n* (with $0 < n < 1$) is a dimensionless parameter determining the degree of deviation from an exact semicircle.[82] When $n = 1$, eq 14 yields the impedance of a capacitor where $A_0 = C$. The resistance *R* can be obtained by considering the intercept of the impedance curve with the Z' axis. Fitting of the semicircles was then performed using the ORIGINLAB software based on the following relationships (eqs 15 and 16):

$$Z' = \frac{R\left(1 + RA_0\omega^n \cos\left(\frac{n\pi}{2}\right)\right)}{1 + 2RA_0\omega^n \cos\left(\frac{n\pi}{2}\right) + (RA_0\omega^n)^2} \tag{15}$$

$$Z'' = \frac{R^2A_0\omega^n \sin\left(\frac{n\pi}{2}\right)}{1 + 2RA_0\omega^n \cos\left(\frac{n\pi}{2}\right) + (RA_0\omega^n)^2} \tag{16}$$

Results about the resistance *R*, the capacitance *C*, and the time constant τ (equivalent to the lifetime of photogenerated charges at the depletion layer of the semiconductor) and equal to the product of the resistance and the capacitance are reported in Table 6.

Increasing the strontium content leads to a progressive increase of the resistance and of the capacitance with the highest values achieved for *R* at 0.4 wt % Sr and for C at about 0.4−0.6 wt % Sr. Increasing further the Sr content leads to a general decreasing trend for both resistance and capacitance values. This general evolution results in a strong increase of the time constant τ with a maximum reached at a loading of 0.4 wt % Sr. The time constant τ is generally considered as an indication of the probability for an electron to recombine with a hole with a higher tendency to recombination increasing with an increase in τ, i.e., the time the electron stays in the depletion layer at the surface of the TiO_2 nanotube semiconductor. Following this reasoning, one should therefore expect recombination to reach a maximum at a Sr loading of 0.4 wt %. This assumption that increasing the time spent by an electron in the depletion layer would increase the probability for this electron to recombine with a hole is therefore in contradiction with the previous kinetic analysis of the photocatalytic results showing an optimum in photocatalytic activity around 0.4 wt % Sr. The τ parameter should in fact be seen as the time necessary to charge or discharge the capacitor

https://doi.org/10.1021/acsomega.2c06717
ACS Omega 2023, 8, 8303−8319

within a given supply percentage. This can be fully expected since the charging (storage) or discharging (release) of a capacitor is not instantaneous. The τ parameter in fact should therefore be envisaged as the time that generated charges can remain at the interface to generate reactive oxygen species (ROS) which will degrade pollutants. Therefore, the increase in τ value with increasing Sr loading up to 0.4 wt % only reflects an improved exciton availability. This leads therefore to a higher probability for these excitons to participate directly or indirectly (by creating reactive oxygen species) in photodegradation reactions. This enhanced availability should be regarded in fact as indicating a higher stabilization of these generated charges related to the implementation of strontium at the surface of the TiO_2 lattice network and inducing a net polarization of the surface of the photocatalytic system. This link between polarization induced by strontium, better stabilization of photogenerated charges, and improved photocatalytic activity will deepen more, emphasized in the next sections.

3.8.2. Determination of Activation Energy. The direct current (dc) conductivity of our systems can be determined using eq 17, where R_b is the bulk resistance calculated in the previous section:[80]

$$\sigma = \frac{e}{SR_b} \tag{17}$$

with S being the area and e the thickness of the pellet.

Multiplying the dc conductivity by the temperature leads to eq 18 following an Arrhenius formula:[83]

$$\sigma T = \sigma_0 \exp\left(\frac{-E_a}{k_B T}\right) \tag{18}$$

with σ_0 being the pre-exponential factor, E_a the activation energy for conduction, k_B the Boltzmann constant, and T the absolute temperature in K.

Linearization of eq 18 gives eq 19:

$$\ln(\sigma T) = \ln(\sigma_0) - \frac{E_a}{k_B T} \tag{19}$$

The Arrhenius plot of the conductivity ($\ln(\sigma T)$ vs $1000/T$) is shown in Figure 11B for the 0.4wt%Sr-Cu-GO-TiNT material. Activation energy is then extracted from the slope of the curve $\ln(\sigma T)$ against reciprocal temperature ($1000/T$). The Arrhenius plots for the other samples of the *x*wt%Sr-Cu-GO-TiNT series as well as of the Sr-free Cu-GO-TiNT reference are reported in Figure S5. The resulting activation energies are then compiled in Table 6.

The addition of strontium as low as 0.2 wt % leads to a significant enhancement of the activation energy from 0.044 eV for the Sr-free Cu-GO-TiNT to 0.16 eV for 0.2wt%Sr-Cu-GO-TiNT. Increasing the Sr content therefore leads to higher values for E_a which is generally considered as an indication for better mobility of photogenerated electron−hole pairs.[74] This enhancement of charge mobility should be a favorable parameter for photodegradation ability since leading to an enhanced effective collision per unit volume as the Sr content increases. However, the activation energy also continues increasing with increasing Sr content with the maximum being achieved at a strontium loading of 0.8 wt %. Therefore, a direct correlation between a higher mobility of photogenerated charges and an enhanced photocatalytic activity is not a sufficient condition for optimized photocatalytic systems. One should however keep in mind that this analysis does not consider any structural modification of the intrinsic optical properties of our materials.

3.8.3. Determination of the Polarizability Properties. Permittivity of a system comprises a real part or dielectric constant (ε') which translates the ability of the medium to be polarized in the presence of the electric field and an imaginary part (ε'' or loss factor) which represents a measure of how dissipative or lossy a material is to an external electric field. The loss tangent is then determined as $\tan\delta = \varepsilon''/\varepsilon'$. If the loss tangent value exceeds 10, this implies that the material studied dissipates too much the energy stored.

The dielectric constant ε' and loss factor ε'' can be calculated directly from results acquired by EIS following eqs 20 and 21:[83]

$$\varepsilon' = -Z''/\omega C_o((Z')^2 + (Z'')^2) \tag{20}$$

$$\varepsilon'' = Z'/\omega C_o((Z')^2 + (Z'')^2) \tag{21}$$

with $C_0 = \varepsilon_0 S/e$ being the capacitance of the void, ε_0 the vacuum permittivity (8.85×10^{-12} F·m^{-1}), S the surface area, and e the thickness of the pellet.

Dielectric constant ε' values were then determined at low (10 kHz, LF) and at high frequency (100 kHz, HF) for each sample as well as the corresponding loss tangent. Values are reported in Table 7.

Table 7. Dielectric Constant (ε') Values Determined at Low (10 kHz) and High (100 kHz) Values and Corresponding Loss Tangent Values for the Series of *x*wt%Sr-Cu-GO-TiNT Samples with $0 \le x \le 1$

		ε'		
wt % Sr	Catalyst	LF	HF	Loss Factor ($\tan\delta$) (100 to 10 kHz)
0	Cu-GO-TiNT	5	8	0.34−0.90
0.2	0.2wt%Sr-Cu-GO-TiNT	8	13	0.35−1.20
0.4	0.4wt%Sr-Cu-GO-TiNT	10	16	0.40−2.20
0.6	0.6wt%Sr-Cu-GO-TiNT	12	17	0.35−1.10
0.8	0.8wt%Sr-Cu-GO-TiNT	11	18	0.50−2.00
1.0	1.0wt%Sr-Cu-GO-TiNT	7	10	0.34−0.90

As shown in Table 7, the addition of strontium as soon as 0.2 wt % leads to an increase of the dielectric constant ε' from 5 to 8 at low frequency and from 8 to 13 at high frequency. Increasing further the Sr content leads to a broad optimum value for ε' at loadings between 0.4 and 0.8 wt %. Finally, at a Sr loading of 1.0 wt %, a significant decrease of the dielectric constant ε' is noticed.

Concomitantly, the loss tangent values are in a low range of values showing that dissipation factors remain limited whatever the sample studied. Therefore, increasing the Sr content up to 0.6−0.8 wt % leads to a substantial enhancement of the polarizability of our materials, showing undoubtedly that the in situ addition of strontium to the TiO_2 semiconductor leads to a better polarized system under an external electric field. This higher ability to be polarized should therefore impact positively the rate of separation of photogenerated electron−hole pairs and enhance the photocatalytic efficiency. This last point was better evaluated in the next section.

3.8.4. Correlation between Photocatalytic Activity and Dielectric Properties. First, comparison between the photocatalytic activity and the ability of our materials to be polarized

https://doi.org/10.1021/acsomega.2c06717
ACS Omega 2023, 8, 8303−8319

was determined at different Sr loadings (Figure 12A) by correlating the variations of the a_1 parameter (see Section 3.7.1) (equivalent to a kinetic rate constant) of the optimized kinetic law as determined in eq 9 with the dielectric constant ε' obtained at low frequency.

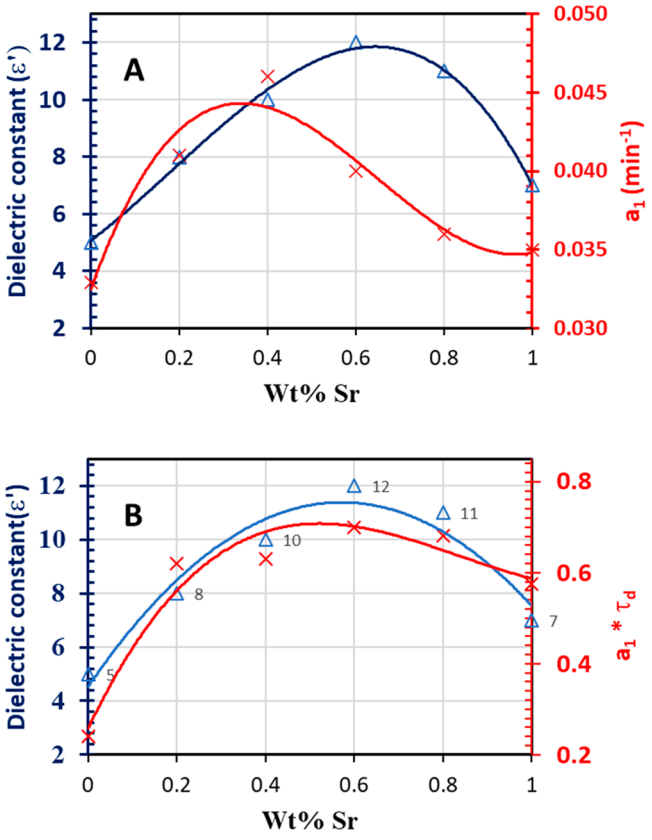

Figure 12. (A) Correlation between the kinetic parameter a_1 and the dielectric constant ε' vs strontium loading. (B) Correlation between the modified kinetic term (a_1*τ_d) including intradiffusion and the dielectric constant ε' vs strontium loading.

As shown in Figure 12A, the increase of the ability to be polarized as characterized by the dielectric constant ε' exhibits a different optimum in Sr loading (0.6 wt %) than the a_1 kinetic parameter. This last observation may be found surprising considering the fact that a higher polarizability of our system is expected to favor a higher separation of photogenerated charges. However, as shown previously, this approach is in fact oversimplistic since kinetic law optimization showed the importance of intradiffusion phenomenon on the kinetic response of our photocatalytic systems.

A way to better ascertain the role of intradiffusion phenomenon is to include the τ_d parameter in the expression of the kinetic response as shown in Figure 12B. Even if approximate, this assumption allows ensuring that intradiffusion is included in the evolution of the kinetic response. Correlating the dielectric constant ε' with this new intradiffusion-containing kinetic parameter leads this time to a perfect correlation between the evolution of the photocatalytic activity and the ability of our system to be polarized. In this way, this correlation validates the fact that the enhancement of the photocatalytic activity as observed here by the addition of strontium is directly related to a higher stabilization of photogenerated charges induced by the ferroelectric polarization of the TiO_2 nanotubes semiconductor.

Further work is in progress to deeply analyze how the ferroelectric polarization induced by strontium enhances the photocatalytic properties of adjacent semiconductors.

4. CONCLUSION

In the present study, the addition of low amounts of strontium to Cu/GO/TiO_2 nanotubes composites was herein deeply analyzed in order to determine its role in the generation of ferroelectric polarization and its potential influence in enhancing the photocatalytic performance of the adjacent TiO_2 nanotube semiconductor. Correlation between a fully optimized description of the kinetic comportment of the composites and dielectric properties clearly showed the role of ferroelectric-induced polarization resulting from the addition of strontium and the formation of Sr-O-Ti entities on the stabilization of photogenerated charges formed onto TiO_2 nanotubes. Better stabilized photogenerated charges are then more available for creating ROS species able to degrade efficiently target pollutant molecules. The approach developed here therefore provides an original methodology able to demonstrate how a fine kinetic analysis of photocatalytic performances can be directly linked to the ability of a given material to be polarized showing in an unambiguous way that polarization can affect in a beneficial way the photocatalytic response.

In a more particular way, this work also demonstrates the role that polarization resulting from a finely controlled addition of a ferroelectric component can play in efficiently enhancing photocatalytic performances in an assisted way without the need of constructing complex photocatalytic systems.

■ ASSOCIATED CONTENT

Supporting Information

The Supporting Information is available free of charge at https://pubs.acs.org/doi/10.1021/acsomega.2c06717.

EDX and EDX mapping measurements for Cu-GO-TiNT and *x*wt%Sr−Cu-GO-TiNT samples; Nyquist diagrams and Arrhenius plots of ln(σT) vs 1000/T for Cu-GO-TiNT, 0.2wt%Sr-Cu-GO-TiNT, 0.6wt%Sr-Cu-GO-TiNT, 0.8wt%Sr-Cu-GO-TiNT, and 1wt%Sr-Cu-GO-TiNT (PDF)

■ AUTHOR INFORMATION

Corresponding Authors

Hafedh Kochkar − *Department of Chemistry, College of Science, Imam Abdulrahman Bin Faisal University, 31441 Dammam, Saudi Arabia; Basic & Applied Scientific Research Center, Imam Abdulrahman Bin Faisal University, 31441 Dammam, Saudi Arabia;* orcid.org/0000-0002-8176-6571; Email: hbkochkar@iau.edu.sa

Gilles Berhault − *Institut de Recherches sur la Catalyse et l'Environnement de Lyon, CNRS−Université Lyon I, 69100 Villeurbanne, France;* orcid.org/0000-0003-4424-3541; Email: gilles.berhault@ircelyon.univ-lyon1.fr

Authors

Nuhad Abdullah Alomair − *Department of Chemistry, College of Science, Imam Abdulrahman Bin Faisal University, 31441 Dammam, Saudi Arabia; Basic & Applied Scientific Research*

https://doi.org/10.1021/acsomega.2c06717
ACS Omega 2023, 8, 8303−8319

Center, Imam Abdulrahman Bin Faisal University, 31441 Dammam, Saudi Arabia

Nouf Saleh Al-Aqeel − *Department of Chemistry, College of Science, Imam Abdulrahman Bin Faisal University, 31441 Dammam, Saudi Arabia; Basic & Applied Scientific Research Center, Imam Abdulrahman Bin Faisal University, 31441 Dammam, Saudi Arabia*

Sanaa Saad Alabbad − *Department of Chemistry, College of Science, Imam Abdulrahman Bin Faisal University, 31441 Dammam, Saudi Arabia*

Muhammad Younas − *Core Research Facilities, King Fahd University of Petroleum and Minerals, 31261 Dhahran, Saudi Arabia*

Fathi Jomni − *Département de Physique, Faculté des Science de Tunis, Université Tunis El Manar, Tunis 1002, Tunisia*

Ridha Hamdi − *Basic & Applied Scientific Research Center, Imam Abdulrahman Bin Faisal University, 31441 Dammam, Saudi Arabia;* orcid.org/0000-0003-1457-9546

Ismail Ercan − *Department of Electrical and Electronics Engineering, Faculty of Engineering, Düzce University, Düzce 81010, Turkey*

Complete contact information is available at: https://pubs.acs.org/10.1021/acsomega.2c06717

Notes

The authors declare no competing financial interest.

■ ACKNOWLEDGMENTS

The authors would like to acknowledge the funding from Ministry of Education (IF-2020-019-BASRC) and Imam Abdulrahman Bin Faisal University, Basic and Applied Scientific Research Center for their support.

■ REFERENCES

(1) Karthikeyan, C.; Arunachalam, P.; Ramachandran, K.; Al-Mayouf, A. M.; Karuppuchamy, S. Recent advances in semiconductor metal oxides with enhanced methods for solar photocatalytic applications. *J. Alloys Compd.* **2020**, *828*, 154281.

(2) Meng, A.; Zhang, L.; Cheng, B.; Yu. Dual Cocatalysts in TiO_2 Photocatalysis. *J. Adv. Mater.* **2019**, *31*, 1807660.

(3) Turki, A.; Guillard, C.; Dappozze, F.; Berhault, G.; Ksibi, Z.; Kochkar, H. Design of TiO_2 nanomaterials for the photodegradation of formic acid - Adsorption isotherms and kinetics study. *J. Photochem. Photobiol. A Chem.* **2014**, *279*, 8−16.

(4) Kumar Kuila, S.; Kumbhakar, P.; Sekhar Tiwary, C.; Kumar Kundu, T. Photon and vibration synergism on planar defects induced 2D-graphitic carbon nitride for ultrafast remediation of dyes and antibiotic ampicillin. *J. Mater. Sci.* **2022**, *57*, 8658−8675.

(5) Turki, A.; Kochkar, H.; García-Fernández, I.; Polo-López, M. I.; Ghorbel, A.; Guillard, C.; Berhault, G.; Fernández-Ibáñez, P. Solar photocatalytic inactivation of *Fusarium Solani* over TiO_2 nanomaterials with controlled morphology - Formic acid effect. *Catal. Today* **2013**, *209*, 147−152.

(6) Parrino, F.; Augugliaro, V.; Camera-Roda, G.; Loddo, V.; López-Muñoz, M. J.; Márquez-Álvarez, C.; Palmisano, G.; Palmisano, L.; Puma, M. A. Visible-light-induced oxidation of *trans*-ferulic acid by TiO_2 photocatalysis. *J. Catal.* **2012**, *295*, 254−260.

(7) Ge, M. Z.; Cao, C. Y.; Huang, J. Y.; Li, S. H.; Zhang, S. N.; Deng, S.; Li, Q. S.; Zhang, K. Q.; Lai, Y. K. Synthesis, modification, and photo/photoelectrocatalytic degradation applications of TiO_2 nanotube arrays: a review. *Nanotechnol. Rev.* **2016**, *5*, 75−112.

(8) Shayegan, Z.; Lee, C. S.; Haghighat, F. TiO_2 photocatalyst for removal of volatile organic compounds in gas phase-A review. *Chem. Eng. J.* **2018**, *334*, 2408−2439.

(9) Meksi, M.; Turki, A.; Kochkar, H.; Bousselmi, L.; Guillard, C.; Berhault, G. The role of lanthanum in the enhancement of photocatalytic properties of TiO_2 nanomaterials obtained by calcination of hydrogenotitanate nanotubes. *Appl. Catal. B Environ.* **2016**, *181*, 651−660.

(10) Clarizia, L.; Vitiello, G.; Luciani, G. I.; Di Somma, I.; Andreozzi, R.; Marotta, R. *In situ* photodeposited nanoCu on TiO_2 as a catalyst for hydrogen production under UV/visible radiation. *Appl. Catal., A* **2016**, *518*, 142−149.

(11) Yao, G. Y.; Zhao, Z. Y.; Liu, Q. L.; Dong, X. D.; Zhao, Q. M. Theoretical calculations for localized surface plasmon resonance effects of Cu/TiO_2 nanosphere: Generation, modulation, and application in photocatalysis. *Sol. Energy Mater. Sol. Cells.* **2020**, *208*, 110385.

(12) Inturi, S. N. R.; Boningari, T.; Suidan, M.; Smirniotis, P. G. Visible-light-induced photodegradation of gas phase acetonitrile using aerosol-made transition metal (V, Cr, Fe, Co, Mn, Mo, Ni, Cu, Y, Ce, and Zr) doped TiO_2. *Appl. Catal. B Environ.* **2014**, *144*, 333−342.

(13) Fotiou, T.; Triantis, T. M.; Kaloudis, T.; O'Shea, K. E.; Dionysiou, D. D.; Hiskia, A. Assessment of the roles of reactive oxygen species in the UV and visible light photocatalytic degradation of cyanotoxins and water taste and odor compounds using C-TiO_2. *Water Res.* **2016**, *90*, 52−61.

(14) Payormhorm, J.; Idem, R. Synthesis of C-doped TiO_2 by sol-microwave method for photocatalytic conversion of glycerol to value-added chemicals under visible light. *Appl. Catal. A Gen.* **2020**, *590*, 117362.

(15) Mittal, A.; Mari, B.; Sharma, S.; Kumari, V.; Maken, S.; Kumari, K.; Kumar, N. Non-metal modified TiO_2: a step towards visible light photocatalysis. *J. Mater. Sci. Mater. Electron.* **2019**, *30*, 3186−3207.

(16) Basavarajappa, P. S.; Patil, S. B.; Ganganagappa, N.; Reddy, K. R.; Raghu, A. V.; Reddy, C. V. Recent progress in metal doped TiO_2, non-metal doped/codoped TiO_2 and TiO_2 nanostructured hybrids for enhanced photocatalysis. *Int. J. Hydrogen Energy.* **2020**, *45*, 7764−7778.

(17) Liu, D.; Jing, L.; Luan, P.; Tang, J.; Fu, H. Enhancement Effects of Cobalt Phosphate Modification on Activity for Photoelectrochemical Water Oxidation of TiO_2 and Mechanism Insights. *ACS Appl. Mater. Interfaces.* **2013**, *5*, 4046−4052.

(18) Li, X.; Lin, H. M.; Chen, X.; Niu, H.; Liu, J. Y.; Zhang, T.; Qu, F. Y. Dendritic α-Fe_2O_3/TiO_2 nanocomposites with improved visible light photocatalytic activity. *Phys. Chem. Chem. Phys.* **2016**, *18*, 9176−9185.

(19) Turki, A.; Kochkar, H.; Guillard, C.; Berhault, G.; Ghorbel, A. Effect of Na content and thermal treatment of titanate nanotubes on the photocatalytic degradation of formic acid. *Appl. Catal., B* **2013**, *138−139*, 401−415.

(20) Tripathy, J.; Lee, K.; Schmuki, P. Tuning the Selectivity of Photocatalytic Synthetic Reactions Using Modified TiO_2 Nanotubes. *Angew. Chem., Int. Ed.* **2014**, *53*, 12605−12608.

(21) Wu, H. B.; Hng, H. H.; Lou, X. W. Direct Synthesis of Anatase TiO_2 Nanowires with Enhanced Photocatalytic Activity. *Adv. Mater.* **2012**, *24*, 2567−2571.

(22) Li, C. J.; Xu, G. R.; Zhang, B. H.; Gong, J. R. High selectivity in visible-light-driven partial photocatalytic oxidation of benzyl alcohol into benzaldehyde over single-crystalline rutile TiO_2 nanorods. *Appl. Catal., B* **2012**, *115*, 201−208.

(23) Meksi, M.; Kochkar, H.; Berhault, G.; Guillard, C. Effect of cerium content and post-thermal treatment on doped anisotropic TiO_2 nanomaterials and kinetic study of the photodegradation of formic acid. *J. Mol. Catal. A Chem.* **2015**, *409*, 162−170.

(24) Giovannetti, R.; Rommozzi, E.; Zannotti, M.; D'Amato, C. A. Recent Advances in Graphene Based TiO_2 Nanocomposites ($GTiO_2Ns$) for Photocatalytic Degradation of Synthetic Dyes. *Catalysts* **2017**, *7* (10), 305.

(25) Leary, R.; Westwood, A. Carbonaceous nanomaterials for the enhancement of TiO_2 photocatalysis. *Carbon* **2011**, *49*, 741−772.

(26) Sampaio, M. J.; Silva, C. G.; Marques, R. R. N.; Silva, A. M. T.; Faria, J. L. Carbon nanotube-TiO_2 thin films for photocatalytic applications. *Catal. Today* **2011**, *161*, 91−96.
(27) Zhang, Y. P.; Xu, J. J.; Sun, Z. H.; Li, C. Z.; Pan, C. X. Preparation of graphene and TiO_2 layer by layer composite with highly photocatalytic efficiency. *Prog. Nat. Sci. Mater. Int.* **2011**, *21*, 467−471.
(28) Meksi, M.; Berhault, G.; Guillard, C.; Kochkar, H. Design of TiO_2 nanorods and nanotubes doped with lanthanum and comparative kinetic study in the photodegradation of formic acid. *Catal. Commun.* **2015**, *61*, 107−111.
(29) Hamandi, M.; Berhault, G.; Dappozze, F.; Guillard, C.; Kochkar, H. Titanium dioxide nanotubes/polyhydroxyfullerene composites for formic acid photodegradation. *Appl. Surf. Sci.* **2017**, *412*, 306−318.
(30) Bin Sadi, A.; AlBilali, R.; Abubshait, S. A.; Kochkar, H. Low temperature design of titanium dioxide anatase materials decorated with cyanuric acid for formic acid photodegradation. *J. Saudi Chem. Soc.* **2020**, *24*, 351−363.
(31) Hamandi, M.; Triki, M.; Llorca, J.; Jomni, F.; Aalomair, N.; Kochkar, H. Investigation of physicochemical and electrical properties of TiO_2 nanotubes/graphene oxide nanocomposite. *Bull. Mater. Sci.* **2020**, *43*, 109.
(32) Adly, M. S.; El-Dafrawy, S. M.; El-Hakam, S. A. Application of nanostructured graphene oxide/titanium dioxide composites for photocatalytic degradation of rhodamine B and acid green 25 dyes. *J. Mater. Res. Technol.* **2019**, *8*, 5610−5622.
(33) Iwase, A.; Ng, Y. H.; Ishiguro, Y.; Kudo, A.; Amal, R. Reduced Graphene Oxide as a Solid-State Electron Mediator in Z-Scheme Photocatalytic Water Splitting under Visible Light. *J. Am. Chem. Soc.* **2011**, *133*, 11054−11057.
(34) Kumbhakar, P.; Pramanik, A.; Biswas, S.; Kole, A. K.; Sarkar, R.; Kumbhakar, P. In-situ synthesis of rGO-ZnO nanocomposite for demonstration of sunlight driven enhanced photocatalytic and self-cleaning of organic dyes and tearstains of cotton fabrics. *J. Hazard. Mater.* **2018**, *360*, 193−203.
(35) Rather, R. A.; Singh, S.; Pal, B. A Cu^{+1}/Cu^0-TiO_2 mesoporous nanocomposite exhibits improved H_2 production from H_2O under direct solar irradiation. *J. Catal.* **2017**, *346*, 1−9.
(36) Xin, B.; Wang, P.; Ding, D.; Liu, J.; Ren, Z.; Fu, H. Effect of surface species on Cu-TiO_2 photocatalytic activity. *Appl. Surf. Sci.* **2008**, *254*, 2569−2574.
(37) Sreekantan, S.; Zaki, S. M.; Lai, C. W.; Tzu, T. W. Disinfection of dairy wastewater effluent through solar photocatalysis processes. *Mater. Sci. Semicond. Process.* **2014**, *26*, 620−631.
(38) Colón, G.; Maicu, M.; Hidalgo, M. C.; Navío, J. A. Cu-doped TiO_2 systems with improved photocatalytic activity. *Appl. Catal. B Environ.* **2006**, *67*, 41−51.
(39) Lalitha, K.; Sadanandam, G.; Kumari, V. D.; Subrahmanyam, M.; Sreedhar, B.; Hebalkar, N. Y. Highly Stabilized and Finely Dispersed Cu_2O/TiO_2: A Promising Visible Sensitive Photocatalyst for Continuous Production of Hydrogen from Glycerol:Water Mixtures. *J. Phys. Chem. C* **2010**, *114*, 22181−22189.
(40) Yu, J.; Hai, Y.; Jaroniec, M. Photocatalytic hydrogen production over CuO-modified titania. *J. Colloid Interface Sci.* **2011**, *357*, 223−228.
(41) Yan, H.; Zhao, T.; Li, X.; Hun, C. Synthesis of Cu-doped nano-TiO_2 by detonation method. *Ceram. Int.* **2015**, *41*, 14204−14211.
(42) Zhu, X. D.; Wen, G. L.; Liu, H.; Han, S. H.; Chen, S. H.; Kong, Q. Q.; Feng, W. One-step hydrothermal synthesis and characterization of Cu-doped TiO_2 nanoparticles/nanobucks/ nanorods with enhanced photocatalytic performance under simulated solar light. *J. Mater. Sci. Mater. Electron.* **2019**, *30*, 13826−13834.
(43) Krishnakumar, V.; Boobas, S.; Jayaprakash, J.; Rajaboopathi, M.; Han, B.; Louhi-Kultanen, M. Effect of Cu doping on TiO_2 nanoparticles and its photocatalytic activity under visible light. *J. Mater. Sci. Mater. Electron.* **2016**, *27*, 7438−7447.
(44) Zghab, E.; Hamandi, M.; Dappozze, F.; Kochkar, H.; Saïd Zina, M.; Guillard, C.; Berhault, G. Influence of graphene and copper on the photocatalytic response of TiO_2 nanotubes. *Mater.Sci. Semicond. Process.* **2020**, *107*, 104847.
(45) Lv, X. J.; Zhou, S. X.; Zhang, C.; Chang, H. X.; Chen, Y.; Fu, W. F. Synergetic effect of Cu and graphene as cocatalyst on TiO_2 for enhanced photocatalytic hydrogen evolution from solar water splitting. *J. Mater. Chem.* **2012**, *22*, 18542−18549.
(46) Cui, Y. F.; Briscoe, J.; Dunn, S. Effect of Ferroelectricity on Solar-Light-Driven Photocatalytic Activity of $BaTiO_3$-Influence on the Carrier Separation and Stern Layer Formation. *Chem. Mater.* **2013**, *25*, 4215−4223.
(47) Yang, W. G.; Yu, Y. H.; Starr, M. B.; Yin, X.; Li, Z. D.; Kvit, A.; Wang, S. F.; Zhao, P.; Wang, X. D. Ferroelectric Polarization-Enhanced Photoelectrochemical Water Splitting in TiO_2-$BaTiO_3$ Core-Shell Nanowire Photoanodes. *Nano Lett.* **2015**, *15*, 7574−7580.
(48) Wu, F.; Yu, Y. H.; Yang, H.; German, L. N.; Li, Z. Q.; Chen, J. G.; Yang, W. G.; Huang, L.; Shi, W. M.; Wang, L. J.; Wang, X. D. Simultaneous Enhancement of Charge Separation and Hole Transportation in a TiO_2-$SrTiO_3$ Core-Shell Nanowire Photoelectrochemical System. *Adv. Mater.* **2017**, *29*, 1701432.
(49) Huang, X. Y.; Wang, K. Q.; Wang, Y. Z.; Wang, B.; Zhang, L. L.; Gao, F.; Zhao, Y.; Feng, W. H.; Zhang, S. Y.; Liu, P. Enhanced charge carrier separation to improve hydrogen production efficiency by ferroelectric spontaneous polarization electric field. *Appl. Catal., B* **2018**, *227*, 322−329.
(50) Chen, F.; Huang, H.; Guo, L.; Zhang, Y.; Ma, T. The Role of Polarization in Photocatalysis. *Angew. Chem., Int. Ed.* **2019**, *58*, 10061−10073.
(51) Zhang, J.; Bang, J. H.; Tang, C.; Kamat, P. V. Tailored TiO_2-$SrTiO_3$ Heterostructure Nanotube Arrays for Improved Photoelectrochemical Performance. *ACS Nano* **2010**, *4*, 387−395.
(52) Liu, Q. H.; Sun, Q.; Zhang, M.; Li, Y.; Zhao, M.; Dong, L. F. Enhanced photoelectrical performance of dye-sensitized solar cells with double-layer TiO_2 on perovskite $SrTiO_3$ substrate. *Appl. Phys. A* **2016**, *122*, 404.
(53) Ouyang, S. X.; Tong, H.; Umezawa, N.; Cao, J. Y.; Li, P.; Bi, Y. P.; Zhang, Y. J.; Ye, J. H. Surface-Alkalinization-Induced Enhancement of Photocatalytic H_2 Evolution over $SrTiO_3$-Based Photocatalysts. *J. Am. Chem. Soc.* **2012**, *134*, 1974−1977.
(54) Li, L.; Liu, X.; Zhang, Y. L.; Salvador, P. A.; Rohrer, G. S. Heterostructured $(Ba,Sr)TiO_3/TiO_2$ core/shell photocatalysts: Influence of processing and structure on hydrogen production. *Int. J. Hydrogen Energy* **2013**, *38*, 6948−6959.
(55) Alrashedi, W.; Kochkar, H.; Berhault, G.; Younas, M.; Ben Ali, A.; Alomair, N. A.; Hamdi, R.; Abubshait, S. A.; Alagha, O.; Gondal, M. F.; Haroun, M.; Tratrat, C. Enhancement of the photocatalytic response of Cu-doped TiO_2 nanotubes induced by the addition of strontium. *J. Photochem. Photobiol. A* **2022**, *428*, 113858.
(56) Watanabe, Y. Ferroelectricity of stress-free and strained pure $SrTiO_3$ revealed by ab initio calculations with hybrid and density functionals. *Phys. Rev. B* **2019**, *99*, 064107.
(57) Nova, T. F.; Disa, A. S.; Fechner, M.; Cavalleri, A. Metastable ferroelectricity in optically strained $SrTiO_3$. *Science* **2019**, *364*, 1075−1079.
(58) Kochkar, H.; Lakhdhar, N.; Berhault, G.; Bausach, M.; Ghorbel, A. Optimization of the Alkaline Hydrothermal Route to Titanate Nanotubes by a Doehlert Matrix Experience Design. *J. Phys. Chem. C* **2009**, *113*, 1672−1679.
(59) Reddy, N. L.; Kumar, S.; Krishnan, V.; Sathish, M.; Shankar, M. V. Multifunctional Cu/Ag quantum dots on TiO_2 nanotubes as highly efficient photocatalysts for enhanced solar hydrogen evolution. *J. Catal.* **2017**, *350*, 226−239.
(60) Morgado, E.; De Abreu, M. A. S.; Moure, G. T.; Marinkovic, B. A.; Jardim, P. M.; Araujo, A. S. Characterization of Nanostructured Titanates Obtained by Alkali Treatment of TiO_2-Anatases with Distinct Crystal Sizes. *Chem. Mater.* **2007**, *19*, 665−676.
(61) Liu, S.; Tian, J.; Wang, L.; Luo, Y.; Sun, X. One-pot synthesis of CuO nanoflower-decorated reduced graphene oxide and its application to photocatalytic degradation of dyes. *Catal. Sci. Technol.* **2012**, *2*, 339−344.

https://doi.org/10.1021/acsomega.2c06717
ACS Omega 2023, 8, 8303−8319

(62) Komaraiah, D.; Radha, E.; James, J.; Kalarikkal, N.; Sivakumar, J.; Reddy, M.V. R.; Sayanna, R. Effect of particle size and dopant concentration on the Raman and the photoluminescence spectra of TiO_2:Eu^{3+} nanophosphor thin films. *J. Lumin.* **2019**, *211*, 320−333.
(63) Cesano, F.; Bertarione, S.; Uddin, M. J.; Agostini, G.; Scarano, D.; Zecchina, A. Designing TiO_2 Based Nanostructures by Control of Surface Morphology of Pure and Silver Loaded Titanate Nanotubes. *J. Phys. Chem. C* **2010**, *114*, 169−178.
(64) Parker, J. C.; Siegel, R. W. Calibration of the Raman spectrum to the oxygen stoichiometry of nanophase TiO_2. *Appl. Phys. Lett.* **1990**, *57*, 943−945.
(65) Scepanovic, M. J.; Grujic-Brojcin, M.; Dohcevic-Mitrovic, Z. D.; Popovic, Z. V. Temperature dependence of the lowest frequency E g Raman mode in laser-synthesized anatase TiO_2 nanopowder. *Appl. Phys. A: Mater. Sci. Process.* **2007**, *86*, 365−371.
(66) Sun, H. Q.; Bai, Y.; Liu, H. J.; Jin, W. Q.; Xu, N. P.; Chen, G. J.; Xu, B. Q. Mechanism of Nitrogen-Concentration Dependence on pH Value: Experimental and Theoretical Studies on Nitrogen-Doped TiO_2. *J. Phys. Chem. C* **2008**, *112*, 13304−13309.
(67) Zhang, H.; Lv, X.; Li, Y.; Wang, Y.; Li, J. P25-Graphene Composite as a High Performance Photocatalyst. *ACS Nano* **2010**, *4*, 380−386.
(68) Ren, W.; Ai, Z.; Jia, F.; Zhang, L.; Fan, X.; Zou, Z. Low temperature preparation and visible light photocatalytic activity of mesoporous carbon-doped crystalline TiO_2. *Appl. Catal., B* **2007**, *69*, 138−144.
(69) Busca, G. FT-IR study of the surface of copper oxide. *J. Mol. Catal.* **1987**, *43*, 225−236.
(70) Praliaud, H.; Mikhailenko, S.; Chajar, Z.; Primet, M. Surface and bulk properties of Cu-ZSM-5 and Cu/Al_2O_3 solids during redox treatments. Correlation with the selective reduction of nitric oxide by hydrocarbons. *Appl. Catal., B* **1998**, *16*, 359−374.
(71) Cao, C. H.; Xiao, L.; Liu, L.; Zhu, H. Y.; Chen, C. H.; Gao, L. Visible-light photocatalytic decolorization of reactive brilliant red X-3B on Cu_2O/crosslinked-chitosan nanocomposites prepared via one step process. *Appl. Surf. Sci.* **2013**, *271*, 105−112.
(72) Schiavoni, M.; Campisi, S.; Carniti, P.; Gervasini, A.; Delplanche, T. Focus on the catalytic performances of Cu-functionalized hydroxyapatites in NH_3-SCR reaction. *Appl. Catal., A* **2018**, *563*, 43−53.
(73) Hierl, R.; Knözinger, H.; Urbach, H. P. Surface properties and reduction behavior of calcined $CuOAl_2O_3$ and $CuO\text{-}NiOAl_2O_3$ catalysts. *J. Catal.* **1981**, *69*, 475−486.
(74) Strohmeier, B. R.; Leyden, D. E.; Field, R. S.; Hercules, D. M. Surface spectroscopic characterization of $CuAl_2O_3$ catalysts. *J. Catal.* **1985**, *94*, 514−530.
(75) Serpone, N.; Lawless, D.; Khairutdinov, R. Size Effects on the Photophysical Properties of Colloidal Anatase TiO_2 Particles: Size Quantization Versus Direct Transitions in This Indirect Semiconductor? *J. Phys. Chem.* **1995**, *99*, 16646−16654.
(76) Liu, J.; Li, J.; Sedhain, A.; Lin, J.; Jiang, H. Structure and Photoluminescence Study of TiO_2 Nanoneedle Texture along Vertically Aligned Carbon Nanofiber Arrays. *J. Phys. Chem. C* **2008**, *112*, 17127−17132.
(77) Lei, Y.; Zhang, L. D.; Meng, G. W.; Li, G. H.; Zhang, X. Y.; Liang, C. H.; Chen, W.; Wang, S. X. Preparation and photoluminescence of highly ordered TiO_2 nanowire arrays. *Appl. Phys. Lett.* **2001**, *78*, 1125−1127.
(78) Preclikova, J.; Galar, P.; Trojanek, F.; Danis, S.; Rezek, B.; Gregora, I.; Nemcova, Y.; Maly, P. Nanocrystalline titanium dioxide films: Influence of ambient conditions on surface and volume-related photoluminescence. *J. Appl. Phys.* **2010**, *108*, 113502.
(79) Hamandi, M.; Berhault, G.; Guillard, C.; Kochkar, H. Reduced graphene oxide/TiO_2 nanotube composites for formic acid photodegradation. *Appl. Catal., B* **2017**, *209*, 203−213.
(80) Almond, D. P.; West, A. R. Impedance and modulus spectroscopy of "real" dispersive conductors. *Solid State Ionics.* **1983**, *11*, 57−64.
(81) Saad, M.; Stambouli, W.; Sdiri, N.; Elhouichet, H. Effect of mixed sodium and vanadium on the electric and dielectric properties of zinc phosphate glass. *Mater. Res. Bull.* **2017**, *89*, 224−231.
(82) Sdiri, N.; Elhouichet, H.; Azeza, B.; Mokhtar, F. Studies of $(90\text{-}x)P_2O_5xB_2O_3.10Fe_2O_3$ glasses by Mössbauer effect and impedance spectroscopy methods. *J. Non. Cryst. Solids.* **2013**, *371−372*, 22−27.
(83) Wu, Z. L.; Sun, L. P.; Xia, T.; Huo, L. H.; Zhao, H.; Rougier, A.; Grenier, J. C. Effect of Sr doping on the electrochemical properties of bi-functional oxygen electrode $PrBa_{1-x}Sr_xCo_2O_{5+\delta}$. *J. Power Sources.* **2016**, *334*, 86−93.

https://doi.org/10.1021/acsomega.2c06717
ACS Omega 2023, 8, 8303−8319